Analysis of the plasma discharge in a Hall thruster via a hybrid 2D code

IEPC-2019-579

Presented at the 36th International Electric Propulsion Conference
University of Vienna, Austria
September 15-20, 2019

A. Domínguez-Vázquez,* J. Zhou,† P. Fajardo‡ and E. Ahedo§
Equipo de Propulsión Espacial y Plasmas, Universidad Carlos III de Madrid, Leganés 28911, Spain

HYPHEN is a new two-dimensional axisymmetric hybrid, particle-in-cell (PIC)/fluid multi-thruster simulation platform under development. This work presents the last modeling advances, outlining the recent improvements incorporated in both the PIC and the electron-fluid segments, and shows the code capabilities regarding the simulation of Hall efect thruster (HET) discharges. Preliminary simulations of a SPT-100 HET are performed in order to assess the code performance and results, and explore the effects of different cathode locations in the near plume region and of various electron turbulent parameter profiles.

I. Introduction

Among the large variety of existing plasma thrusters, the Hall effect thruster (HET) constitutes a well-established, reliable and successfully flown technology.[1–5] On the other hand, new promising technologies such as the helicon plasma thruster[6–13] (HPT) or the electron-cyclotron-resonance thruster[14–19] (ECRT) are under current development. Therefore, there is a need for a versatile multi-thruster simulation platform aiming at (*i*) facilitating and complementing the design of new prototypes, (*ii*) revealing optimization opportunities so as to improve the thruster performance and lifetime, and (*iii*) providing a deeper insight into relevant still open problems in already proven technologies.

Gathering the advantages of both particle-in-cell (PIC) and fluid models,[20,21] and based on the broad expertise on HET simulation gained with previous codes such as HPHall,[22] HPHall-2[23] or HallMA,[24] our research group has developed HYPHEN,[25] standing for HYbrid Plasma thruster Holistic simulation ENvironment: a new two-dimensional axisymmetric hybrid PIC-fluid code devoted to the simulation of the plasma physics inside the chamber and in the near plume of various plasma thrusters. Although the focus of this work is on HET simulations, HYPHEN has been recently extended to the simulation of HPT[26–28] and ECRT,[29,30] and it is also able to simulate axisymmetric plasma plumes.[31–33]

Regarding HET simulations, HYPHEN incorporates numerous improvements in both the PIC and the electron-fluid segments which significantly increase its capabilities with respect to the aforementioned previous simulation HPHall, HPHall-2 or HallMA. The PIC model allows to independently characterize populations featuring very different dynamics, such as the injected neutral gas and the singly and doubly charged ions, yielding noise-limited estimates of their macroscopics magnitudes thanks to a new efficient population control based on generation weights.[25,31–33]

On the other hand, the electron-fluid model for HETs is named NOMADS, standing for NOn-structured Magnetically Aligned plasma Discharge Simulator, and it solves a fully 2D axisymmetric fluid formulation for the electron population in a Magnetic Field Aligned Mesh (MFAM), which permits (*i*) the simulation of complex magnetic topologies featuring magnetic field singular points or magnetically shielded regions present

*PhD student, Bioengineering and Aerospace Engineering Department, addoming@ing.uc3m.es.
†PhD student, Bioengineering and Aerospace Engineering Department,jzhou@pa.uc3m.es
‡Professor, Bioengineering and Aerospace Engineering Department,pfajardo@ing.uc3m.es
§Professor, Bioengineering and Aerospace Engineering Department,eahedo@ing.uc3m.es

in new HET designs,[34–37] and (*ii*) the extension of the domain boundaries for assessing the plasma physics in the near plume region, thus enabling the synergy with plasma plume codes such as EP2PLUS.[38] It was originally developed by Pérez-Grande,[39,40] has been recently improved by Domínguez-Vázquez[25] for the case of an isotropic electron pressure tensor. Two remarkable improvements are related to (*i*) the treatment of the volumetric cathode model,[41] which allows to assess the effects on the discharge of the cathode location in the near plume region, and (*ii*) the identification of three different turbulent contributions acting on the electron momentum, energy and heat flux equations, which are modeled through three different electron turbulent parameters α_{tm}, α_{te} and α_{tq}, respectively, according to the collisional version of the (collisionless) electron turbulent transport.[22,42–45] Although this approach cannot help in the understanding of the physical mechanism behind the enhanced electron transport reported by experiments, it allows the incorporation to the electron-fluid equations of effective electron cross-field mobility models obtained from kinetic studies.[46–50]

With the main purpose of assessing the HYPHEN performance and revealing its capabilities and limitations, this work presents several studies performed in a typical SPT-100 HET simulation scenario. First, the well-known breathing mode oscillation in the range of 10-30 kHz characterizing the typical HET operation[42,51–53] is identified in a reference simulation case. Second, the effects on the discharge of the cathode location in the near plume region are analyzed so as to assess the validity of the axisymmetric volumetric cathode model. Finally, regarding the yet not well understood electron anomalous transport in HETs, Jorns[43] has recently provided advanced fittings for the electron momentum turbulent parameter through data-driven machine learning techniques, and multi-fluid simulations performed by Mikellides and Ortega[44] have accurately reproduced experimental measurements using a multiple-coefficient approach for the spatial profile of the turbulent parameter acting on the electron momentum equation. Following previous studies,[22–24,39,40,54,55] this work shows preliminary results considering an unique electron turbulent parameter $\alpha_t = \alpha_{tm} = \alpha_{te} = \alpha_{tq}$ featuring constant values and step-out profiles.

The structure of the manuscript is the following. The code structure and main simulation loop are described in Sec. II. The main characteristics of both the PIC and the electron-fluid models are summarized in Secs. III and IV, respectively. The simulation results are presented and discussed in detail in Sec. V. Finally, the conclusions are drawn in Sec. C.

II. Code structure and main simulation loop

HYPHEN overall architecture and structure are based on modularity, aiming to be a more flexible and capable simulation platform potentially extensible to HPT[26–28] or ECRT,[29,30] as well as HET. In order to maximize code sharing and standardization, HYPHEN has been designed with the same overall architecture, data structure and interfaces as those of the hybrid 3D plasma plume code EP2PLUS, developed by Cichocki,[38,56–58] so that it is also able to simulate axisymmetric plasma plumes.[25,32,33] The different programming languages used are Python/Matlab for data pre and post-processing and results analysis, and Fortran for the main numerical computations. Additionally, industry-level standards such as HDF5 technology for high-performance data management and Open-MP for code parallelization are considered, the code development process following a strict Test Driven Design (TDD) philosophy.

Figure 1 sketches the code structure and main simulation loop. The code consists of three main modules: the PIC module, which follows a Lagrangian approach for simulating the dynamics of the heavy species (i.e. ions and neutrals), the electron module, that considers a fluid model for the electrons, and a sheath module that provides the proper coupling between the quasineutral plasma and the thruster walls by solving the non-neutral plasma sheaths that develop around them, which are treated as surface discontinuities by the quasineutral plasma simulator.

The PIC module takes as inputs the externally applied magnetic field $\boldsymbol{B}$, the electric potential ϕ and the electron temperature T_e, and performs the injection, collisions and propagation of the heavy species one simulation timestep forward, computing the plasma production through the ionization of the injected neutral gas and obtaining, for each heavy species s, the particle density n_s and flux $\boldsymbol{g}_s$ through a particle-to-mesh weighting process. The electron-fluid module, taking those values from the PIC module and considering quasineutrality (i.e. $n_e = \sum_{s \neq e} Z_s n_s$, with Z_s the charge number of the species s), solves a given fluid model of the electron population computing the electric potential and the electron population related variables (e.g. the electron temperature and current density vector $\boldsymbol{j}_e$), thus closing the loop. However, in general, each of those central modules operates on a different mesh of the simulation domain: a structured mesh for the PIC module (referred to as the PIC mesh hereafter), and an unstructured MFAM for the electron-fluid module [see

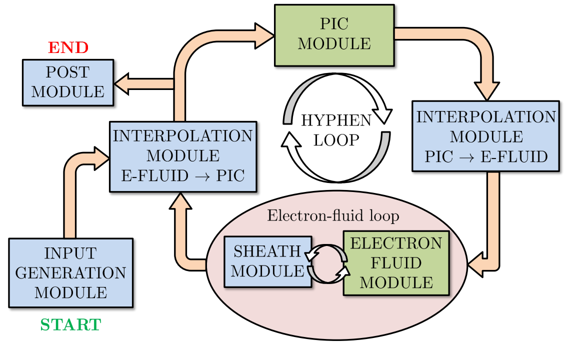

Figure 1. HYPHEN general simulation loop.

Fig. 2(b)]. Therefore, both modules communicate each other through a dedicated bidirectional interpolation module. Finally, the input generation and the post modules are in charge of pre and post-processing tasks, respectively.

III. The PIC model

The PIC model structure and algorithms are described in detail in Refs. 25, 31–33, 57. Here a brief summary of the main features is provided. Aiming at the improvement of the heavy species PIC-related statistics and the extension of the code capabilities, the HYPHEN versatile PIC module groups the different ion and neutral macroparticles into dedicated populations or particle lists storing all necessary particle data such as its position and velocity, elementary mass and charge status, and particle weight (or number of elementary particles represented by each simulation particle). This subdivision of the different species facilitates the population control during the simulation and the treatment of the various particle collisions between different particle lists, thus contributing to reduce the PIC numerical noise.

Taking advantage of its higher computational efficiency in terms of macroparticle sorting algorithms, the PIC module operates in a structured mesh of the axisymmetric simulation domain [see Fig. 2(a)], its boundaries representing 3D annular surfaces and the quadrilateral cells corresponding to 3D annular volumes. Non-trivial cylindrical effects have been successfully cancelled through corrected particle generation and weighting algorithms, and a new population control based on generation weights allows to independently monitorize every simulated population, maintaining the number of particles per cell within a prescribed range and limiting the macroparticle weights dispersion at a low computational cost.[25, 33]

The PIC module up-to-date optimized algorithms for the heavy species treatment can be classified into two types: *particle-wise* and *mesh-element-wise* algorithms. The former are applied to every simulated macroparticle and include (*i*) interpolation of electromagnetic fields to the macroparticle position, (*ii*) integration of the macroparticle trajectory updating its velocity and position with a leap-frog algorithm, (*iii*) check for particle-surface crosses, and (*iv*) macroparticle sorting to the mesh cells. The latter are run for each PIC mesh volume cell or cell face and comprise (*i*) the collisional processes involving the heavy species particles, such as the ionization collisions, (*ii*) the volumetric weighting of sorted macroparticles, (*iii*) the particle-surface interactions including the injection of new particles into the simulation domain, the ion recombination and neutral reinjection and reflection at material walls, and the surface weighting of both the wall-emitted and wall-hitting macroparticles in order to update their related macroscopic magnitudes at the corresponding boundary cell faces, (*iv*) the Bohm condition forcing at the quasineutral material boundaries, and (*v*) the update of the macroparticle generation weight for each simulated heavy species population to appropriately control the number of macroparticles per cell within a specified interval in stationary conditions.

Finally, as for the collisions affecting the heavy species, only singly and doubly ionization collisions are considered here, the ionization rates following the Drawin[59] and Bell[60] models for the reactions $A + e \rightarrow A^+ + 2e$ and $A + e \rightarrow A^{++} + 3e$, and $A^+ + e \rightarrow A^{++} + 2e$, respectively, and the corresponding algorithm based on that of HPHall.[22]

IV. The electron-fluid model

The complete description of the electron-fluid module for HETs can be found in Ref. 25, and it is here briefly outlined. As mentioned in Sec. II, every simulation step, after the PIC segment execution and applying quasineutrality, the current continuity and the electron momentum equations are solved together for updating the electric potential and the electron current density vector, while the electron temperature and heat flux vector are updated separately from the electron energy and heat flux equations.

A. The current continuity and the electron momentum equations

Adding the contributions of all the heavy species and considering quasineutrality, the current continuity equation is

$$\nabla \cdot \boldsymbol{j} = -eS_e, \tag{1}$$

where $\boldsymbol{j} = \boldsymbol{j}_e + \boldsymbol{j}_i$, $\boldsymbol{j}_e = -en_e\boldsymbol{u}_e$ and $\boldsymbol{j}_i = e\sum_{s\neq e} Z_s n_s \boldsymbol{u}_s$ are, respectively, the total, electron and ion current densities, the latter given by the PIC module, with $\boldsymbol{u}_e$ and $\boldsymbol{u}_s = \boldsymbol{g}_s/n_s$ the drift velocities of the electron and heavy species s. The term $S_e = n_e\nu_{cat}$ in the right hand side of Eq. (1) represents the electron source term corresponding to the electron injection through the volumetric cathode,[41] which is the only net source of electrons, ν_{cat} being the cathode equivalent electron emission frequency, so that the total electron current emitted by the cathode (i.e. the discharge current) is

$$I_d = e\int_{V_{cat}} n_e \nu_{cat} dV, \tag{2}$$

where the integral extends to the volumetric cathode region, featuring a volume V_{cat}. It is stressed that $\nu_{cat} = 0$ outside the volumetric cathode region, and that at the current state of development, the cathode is represented by a single MFAM cell located in the near plume region, as shown in Fig. 2(b).

The transport equations for the magnetized electron population are solved in an MFAM so as to mitigate the strong numerical diffusion arising from the $\boldsymbol{B}$-induced large anisotropy between the $\boldsymbol{B}$-parallel and perpendicular electron transport properties.[61] An orthonormal magnetic reference system $\{\mathbf{1}_\parallel, \mathbf{1}_\theta, \mathbf{1}_\top\}$ locally aligned with the dominant stationary externally applied magnetic field is defined, with $\mathbf{1}_\parallel = \boldsymbol{B}/B$ and $\mathbf{1}_\top = \mathbf{1}_\parallel \times \mathbf{1}_\theta$ the B-parallel and perpendicular versors, respectively. Projecting in the above magnetic reference system, neglecting the electron inertia and considering the collisional version of the electron turbulent effects in the momentum detailed in Ref. 25, the generalized Ohm law for the electron current density is

$$j_{\parallel e} = \sigma_e \left(\frac{1}{en_e} \frac{\partial (n_e T_e)}{\partial \mathbf{1}_\parallel} - \frac{\partial \phi}{\partial \mathbf{1}_\parallel} \right) - j_{\parallel c}, \tag{3}$$

$$j_{\top e} = \frac{\sigma_e}{1+\chi\chi_{tm}^*} \left(\frac{1}{en_e} \frac{\partial (n_e T_e)}{\partial \mathbf{1}_\top} - \frac{\partial \phi}{\partial \mathbf{1}_\top} \right) - \frac{j_{\top c} + \chi_{tm}^* j_{\theta c}}{1+\chi\chi_{tm}^*}, \tag{4}$$

$$j_{\theta e} = -\chi_{tm}^* j_{\top e} - \frac{\chi_{tm}^*}{\chi} j_{\theta c}, \tag{5}$$

where the electron temperature is expressed in energy units,

$$\boldsymbol{j}_c = \frac{en_e}{\nu_e} \sum_{s\neq e} \nu_{es} \boldsymbol{u}_s \tag{6}$$

is the total heavy species equivalent collisional current density, contributing to the electron resistivity, with $\nu_e = \sum_{s\neq e} \nu_{es} + \nu_{cat}$ the total electron collision frequency, which adds the different collision frequencies ν_{es} of the electrons with other species s (i.e. elastic and ionization collisions depending on n_e and T_e) as well as the cathode contribution, $\sigma_e = e^2 n_e/(m_e\nu_e)$ is the electron parallel conductivity, $\chi = \omega_{ce}/\nu_e$ and $\chi_{tm}^* = \chi/(1+\alpha_{tm}\chi)$ are the classical Hall parameter and the effective one acting on the electron momentum equation, respectively, with $\omega_{ce} = eB/m_e$ the electron cyclotron frequency, and

$$\alpha_{tm} = \frac{\langle n_e' E_\theta' \rangle}{n_e u_{\theta e} B} \tag{7}$$

is the electron turbulent parameter acting on the momentum equation, where n'_e and E'_θ represent the electron density and azimuthal electric field fluctuations with respect to their time and azimuthal-averaged values, and $\langle\ \rangle$ means averaging on both t and θ. (see Ref. 25 for further details).

Given a T_e profile, Eqs. (1) and (3)-(5) are jointly solved for ϕ and $\boldsymbol{j_e}$ through a cell centered finite volume method (CC-FVM) in a non-structured MFAM, which requires the application of gradient reconstruction (GR) techniques to express the value of a function and its derivatives at the face centers in terms of its values at the cell centers, which are the actual computational points. The weighted least squares (WLSQ) method introduced by Sozer[62] has been implemented in NOMADS.[39,40,61]

Regarding the boundary conditions, $\boldsymbol{j}\cdot\boldsymbol{n} = 0$, with $\boldsymbol{n}$ the boundary normal versor pointing outwards, is set at the dielectric thruster walls and symmetry axis [red and magenta lines in Fig. 2(a), respectively] and at the downstream free loss boundary (current free condition for the expanding plasma plume leaving the domain) represented by the blue lines in Fig. 2(a). Regarding the former, the sheath model developed by Ahedo and de Pablo,[63] which accounts for (i) the secondary electron emission (SEE) from the dielectric walls including elastically reflected and true-secondary electrons and (ii) the partial thermalization or replenishment of the primary electrons velocity distribution function (VDF) through a parameter σ_t (not to be mistaken with the electron parallel conductivity σ_e) provides the corresponding sheath potential fall, to be considered for computing the electron and ion species wall energy losses. At the conducting anode wall depicted in green in Fig. 2(a), for each MFAM boundary cell face m, a linearized sheath model[40] provides a relation between the wall-collected net current density and the sheath potential drop $\Delta\phi_{sh,m} = \phi_m - \phi_A$ with ϕ_m and ϕ_A the electric potential at the face m and at the anode wall, respectively. Considering the usual HET constant voltage operation, I_d in Eq. (2) is unknown, and a given discharge voltage V_d is set between the anode and the cathode, so that

$$V_d = \phi_A - \phi_{cat}, \tag{8}$$

where ϕ_{cat} is the cathode potential. For simplicity, we set the cathode as the reference potential point, so that $\phi_{cat} = 0$ and $\phi_A = V_d$. An iterative process is set on the values $\Delta_{sh,m}$ until the obtained electric potential solution satisfies the current continuity equation in Eq. (1) within a given tolerance.

Although electron inertial effects are not explicitly included in the model, the electron drift-to-internal energy ratio $m_e u_e^2/2T_e$, with $u_e \equiv |\boldsymbol{u}_e|$, has been limited to a given tolerance so that unbounded drift velocities presumably arising not only around the anode, but also in the near plume regions[64,65] are avoided.

B. The electron energy and heat flux equations

The electron internal energy equation reads

$$\frac{\partial}{\partial t}\left(\frac{3}{2}n_e T_e\right) + \nabla\cdot\left(\frac{5}{2}n_e T_e \boldsymbol{u}_e + \boldsymbol{q}_e\right) = \boldsymbol{u}_e\cdot\nabla(n_e T_e) + \frac{\chi}{\chi_{te}^*}\sigma_e^{-1} j_e^2 + \sigma_e^{-1}\boldsymbol{j}_e\cdot\boldsymbol{j_c} + Q_e - \frac{1}{2}m_e u_e^2 S_e, \tag{9}$$

where (i) $\boldsymbol{q}_e$ is the electron heat flux vector; (ii) the electron mass and energy source/sink terms are, respectively, $m_e S_e = m_e n_e(\nu_e^{ion} + \nu_{cat})$, with ν_e^{ion} the total ionization collision frequency, and $Q_e = Q_{ion} + Q_{ex} + 3n_e\nu_{cat}T_{cat}/2$, T_{cat} being the temperature of the electrons emitted from the volumetric cathode in energy units, and $Q_{ion}, Q_{ex} < 0$ the energy sink terms due to the ionization and excitation collisions; and (iii) $\chi_{te}^* = \chi/(1+\alpha_{te}\chi)$ is the effective Hall parameter acting on the electron internal energy equation, with

$$\alpha_{te} = -\frac{\langle u'_{\theta e}E'_\theta\rangle}{u_e^2 B}, \tag{10}$$

the corresponding turbulent parameter, $u'_{\theta e}$ standing for the electron azimuthal drift velocity fluctuations.

In order to close the set of fluid equations for the electron population, a generalized Fourier law for the electron heat flux, analogous to the Ohm law in Eqs. (3)-(5) is considered:

$$q_{\parallel e} = -k_e\frac{\partial T_e}{\partial \boldsymbol{1}_\parallel} - \frac{5T_e}{2e}(j_{\parallel e} + \mathrm{j}_{\parallel c}), \tag{11}$$

$$q_{\top e} = -\frac{k_e}{1+\chi\chi_{tq}^*}\frac{\partial T_e}{\partial \boldsymbol{1}_\top} + \frac{5T_e}{2e(1+\chi\chi_{tq}^*)}\left[(\chi\chi_{tq}^* - 1)j_{\top e} - j_{\top c}\right], \tag{12}$$

$$q_{\theta e} = -\chi_{tq}^* q_{\top e} + \frac{5T_e}{2e}\chi_{tq}^* j_{\top e}, \tag{13}$$

where $k_e = 5T_e\sigma_e/2e^2$ is the electron parallel thermal conductivity, and $\chi_{tq}^* = \chi/(1+\alpha_{tq}\chi)$ is the effective Hall parameter acting on the electron heat flux equation, with

$$\alpha_{tq} = -\frac{5}{2}\frac{\langle p_e' E_\theta' \rangle}{q_{\theta e} B}, \tag{14}$$

the corresponding turbulent parameter, p_e' standing for the electron pressure (i.e. $p_e = n_e T_e$) fluctuations.

Given the solution for ϕ and $\boldsymbol{j}_e$ from Eqs. (1) and (3)-(5), Eqs. (9) and (11)-(13) are solved for updating T_e and $\boldsymbol{q}_e$ with the following boundary conditions: $\boldsymbol{q}_e \cdot \boldsymbol{n} = 0$ is imposed at the symmetry axis and at the downstream free loss boundary, the latter representing an adiabatic condition for the expanding plasma plume at infinity; at the anode and dielectric thruster walls, the total electron energy flux represented by the second member in the left hand side of Eq. (9) is given by the aforementioned corresponding sheath model.

Finally, Eq. (9) is discretized in time according to the semi-implicit approach described in Ref. 40, which allows to keep a linear system of equations, amenable to be solved through the parallel direct solver PARDISO.[66,67] A number N_{ke} of sub-iterations is performed per simulation or PIC timestep.

V. Simulations

A. Simulation settings

Figures 2(a) and 2(b) show the PIC mesh and the MFAM of the typical simulation domain of a SPT-100 HET. The dimensions of the thruster chamber and near plume region, which includes the symmetry axis are listed in Table 1, along with the main meshes characteristics and the most relevant simulation parameters. Figure 2(b) shows the different volumetric cathode locations analyzed in detail in Sec. V.B.1, being their coordinates collected in Table 1. The cathode position C1 corresponds to the reference case here described, located in the same magnetic field streamline as C2 and C3. On the other hand, the cathode position C4 is on the last closing magnetic field streamline in the simulation domain. The cathode electron emission temperature is set to 3 eV for all the cases simulated. As mentioned in Sec. IV.A, the reference for the electric potential (i.e. the point where $\phi = 0$) is set at the center of the MFAM cell representing the volumetric cathode for each case. The base magnetic circuit configuration presented in Ref. 40 for the SPT-100 is considered here for all the cases simulated. The magnetic field intensity and the axial profile of the magnetic field intensity along the simulation domain at a radius $r = 4.63$ cm are shown in Figs. 2(c) and 2(d), respectively. The value of the maximum magnetic field intensity and its axial location at the thruster center line (TCL), along with the average magnetic field intensity at the free loss boundary downstream [vertical blue boundary line in Fig. 2(a)] are listed in Table 1.

Here, the nominal SPT-100 HET operation parameters reported in Ref. 68, already considered by Pérez-Grande,[39,40] are adopted. The constant voltage operation mode is simulated for all cases with a discharge voltage $V_d = 300$ V. Assuming xenon as propellant, a neutral mass flow $\dot{m}_A = 5$ mgs^{-1} is injected from a Maxwellian reservoir through the whole annular anode wall located at $z = 0$ [green left boundary in Fig. 2(a)] featuring a flat profile with a sonic axial velocity based on its own temperature (see Table 1). Singly and doubly charged ions are generated through the ionization of both the injected and the recombined neutrals at the thruster ceramic walls [red boundary lines in Fig. 2(a)], according to the ionization reactions commented in Sec. III. The ion-recombined neutrals are diffusely emitted from the material walls considering complete accommodation of the impacting ions, as suggested by several authors.[54,69] Thus, the neutral emission energy is only given by the wall temperature, which is set to 850 K. Neutrals are diffusely reflected with zero neutral-wall accommodation at the material walls.

All the simulations feature three different particle populations independently monitorized and identified as follows: n grouping both the injected and recombined Xe neutrals, $i1$ containing the singly charged ions Xe^+ generated from the ionization of n, and $i2$ corresponding to the doubly charged ions Xe^{++} from the ionization of both n and $i1$. Regarding the population control algorithm, a target number of macroparticles per cell of 500 is considered per particle population, with a control range of $\pm 10\%$.

The simulation (or PIC) timestep (see Table 1) is set so that a doubly charged ion accelerated across the discharge voltage takes at least two simulation timesteps to cross the smallest PIC mesh cell. Every simulation features a total of 60000 simulation steps (equivalent to 900 μs of simulation time), and is divided in two phases. First, an initialization phase of 15000 simulation steps (equivalent to 225 μs of simulation time) provides an initial state solution for NOMADS considering isothermal electrons with $T_e = 8$ eV, the electric potential obtained from the collisionless electron momentum balance equation as $e\phi/T_{e0} = \ln(n_e/n_{e0})$,

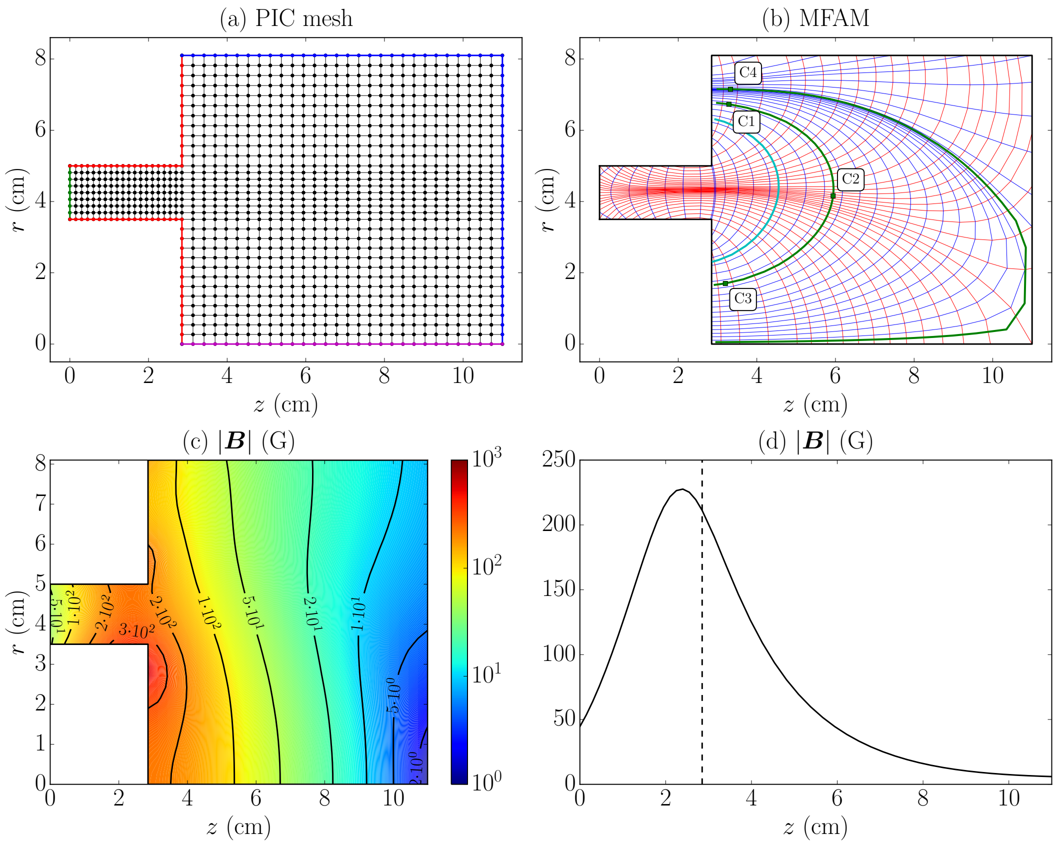

Figure 2. (a) The PIC mesh. The red, green, blue and magenta lines indicate the thruster dielectric walls, the anode wall, the free loss boundary and the symmetry axis at $r = 0$, respectively. (b) The MFAM used by NOMADS. The blue and red MFAM faces defining the MFAM cells are aligned along the magnetic field parallel and perpendicular directions, respectively. The green squares indicate the various volumetric cathode positions considered, whose coordinates are listed in Table 1. The location C1 is considered for the reference case. The green lines correspond to the magnetic field streamlines passing through the different cathode positions, C1, C2 and C3 being upon the same magnetic line. The cyan line marks an additional magnetic field streamline dealt with in Sec. V.B.1. (c) The magnetic field intensity. (d) The axial profile of the magnetic field intensity at a radius $r = 4.63$ cm. The dashed vertical line indicates the axial location of the thruster chamber exit plane, at $z = 2.85$ cm (see Table 1).

where n_{e0} and T_{e0} are the electron density and temperature at the point where $\phi = 0$, respectively. Starting from the initial solution above, a second phase featuring 45000 simulation steps (i.e. 675 μs of simulation time) using NOMADS for the electron population completes the simulation, the obtained discharge current undergoing around seven oscillations reproducing the HET breathing mode. An appropriate value of $N_{ke} = 5$ NOMADS time sub-iterations per simulation step is considered (refer to Ref. 25 for further details). All the results shown in the following sections are time-averaged over 50 simulation timesteps (equivalent to $7.5 \cdot 10^{-1}$ μs of simulation time), which allows for a proper visualization while still reproducing oscillation modes of interest. Furthermore, a time-averaging over the last 450 μs of simulation time (time enough for the discharge current to perform around five complete oscillations) is performed for all the time-averaged variables shown in the following sections.

All the simulation cases consider an electron turbulent parameter $\alpha_t = \alpha_{tm} = \alpha_{te} = \alpha_{tq}$, so that $\chi^* = \chi^*_{tm} = \chi^*_{te} = \chi^*_{tq}$ is the effective Hall parameter. While the results for different α_t values and profiles are shown in Sec. V.B.2, the reference simulation case takes $\alpha_t = 2.5 \cdot 10^{-2}$, so that the effective electron collision frequency $\nu^*_e = \nu_e + \alpha_t \omega_{ce}$, with $\nu_e \sim 10^6$, is dominated by the B-proportional turbulent contribution $\alpha_t \omega_{ce} \sim 10^7$, and limits the effective Hall parameter to $\chi^* \sim 35$.

As for the electron inertial effects (refer to Sec. IV.A), the magnitude of the electron drift velocity is limited to twice the electron thermal one, so that the electron drift-to-internal energy ratio $m_e u_e^2/2T_e$, with $u_e \equiv |\boldsymbol{u}_e|$, can take a maximum value of two.

Simulation parameter	Units	Value
Thruster chamber length, L	cm	2.85
Thruster chamber inner radius, r_1	cm	3.50
Thruster chamber outer radius, r_2	cm	5.00
Near plume region length	cm	8.15
Near plume region radius	cm	8.10
PIC mesh number of cells, nodes	-	1080, 1161
PIC mesh spacings in chamber Δz, Δr	mm	1.50, 1.88
PIC mesh spacings in near plume Δz, Δr^*	mm	2.81, 2.53
MFAM number of cells, faces	-	1173, 2411
MFAM average cells skewness[40]	-	$2 \cdot 10^{-2}$
MFAM average aspect ratio[40]	-	10^{-1}
C1 cathode location, z, r	cm	3.29, 6.73
C2 cathode location, z, r	cm	5.94, 4.16
C3 cathode location, z, r	cm	3.20, 1.70
C4 cathode location, z, r	cm	3.33, 7.15
Cathode emission temperature, T_{cat}	eV	3
Cathode volume C1, C2, C3, C4	cm^3	1.68,0.697,0.854,0.138
Max. $\|\boldsymbol{B}\|$ along the TCL	G	242.75
Axial location of max. $\|\boldsymbol{B}\|$ at the TCL	cm	2.40
Average $\|\boldsymbol{B}\|$ at the free loss exit plane	G	5.04
Discharge voltage, V_d	V	300
Simulation (PIC) timestep, Δt	s	$1.50 \cdot 10^{-8}$
Total number of simulation steps	-	60000
Number of initialization steps	-	15000
Number of simulation steps with NOMADS	-	45000
Injected Xe velocity	ms^{-1}	300 (sonic)
Injected Xe temperature	eV	$7.35 \cdot 10^{-2}$
Injected Xe mass flow, $\dot{m}_A$	mgs^{-1}	5

Table 1. Main simulation parameters of the SPT-100 HET reference simulation case. The radial PIC mesh spacing marked with an asterisk (*) represents the average radial spacing in the near plume region.

Regarding the parameters for the sheath model at the thruster dielectric walls (refer to Sec. IV.A), Boron Nitride data for the SEE is taken from Ref. 63, while $\sigma_t = 0.3$ is considered for all the cases presented here. It is underlined that the metallic anode features no SEE.

The simulations here described considered a total number of particles of around one million, a parallel 10 threads simulation requiring a total computational time of around 17 hours in an up-to-date workstation.

B. Simulation results and discussion

1. *Reference case and cathode location effects*

In this section the results for the reference simulation case with cathode location at C1 described in Sec. V.A are first discussed in detail and then compared to those of the simulation cases featuring cathode locations at C2, C3 and C4, depicted in Fig. 2(b), keeping constant the rest of simulation parameters. Table 2 lists the relevant data of the discharge for each simulation case, which shall be commented on this section along with Figs. 3-7. Figures 4 and 5 show the time-averaged axial profiles at $r = 4.63$ cm of different magnitudes characterizing the discharge for the cases C1-C4. The vertical black dashed, dot-dashed and dotted lines in Figs. 4 and 5 indicate, respectively, the axial position of the thruster chamber exit plane at $z = 2.85$ cm and

Variable	Units	C1	C2	C3	C4
$\bar{n}_e$	10^{17} m^{-3}	1.53	1.51	1.53	1.40
$\bar{n}_n$	10^{17} m^{-3}	7.51	7.17	7.26	8.03
I_d	A	6.41	6.78	6.62	6.01
$I_{i\infty}$	A	4.84	4.98	4.89	4.74
η_{thr}, η_u	-	0.28, 0.97	0.32, 0.97	0.30, 0.95	0.37, 0.95
η_{cur}, η_{div}, η_{prod}	-	0.76, 0.83, 0.62	0.73, 0.85, 0.62	0.74, 0.84, 0.61	0.79, 0.81, 0.64
I_{sp}, F	s, mN	1508, 73.96	1646, 80.74	1578, 77.39	1667, 81.47
P_d, P_{use}	W	1924, 654	2028, 766	1986, 717	1803, 780
P_{walls}, $P_{ion,ex}$	W	1032, 162	1028, 172	1055, 171	801, 157
ν_{cat}	MHz	462	154	340	16354

Table 2. Main results for the simulation cases C1-C4. Time-averaged values over the number of complete cycles within the last 450 μs of simulation time.

the axial position of the magnetic field streamlines passing through the cathode positions C1-C3 at $z = 5.94$ cm, and C4 at $z = 9.69$ cm. Figure 6 shows time-averaged 2D contour maps of different magnitudes for the case C1. Moreover, Fig. 7 depicts time-averaged 2D magnitude contour plots and streamlines of the 2D (z, r) electron and ion current densities $\tilde{\boldsymbol{j}}_e$ and $\tilde{\boldsymbol{j}}_i$ for the cases C1-C4. The black square marker indicates the cathode position for each case in Figs. 6 and 7.

The main features of the plasma discharge are first analyzed focusing on the case C1. The ionization induced predator-prey type fluctuation characterizing the typical HET breathing mode is revealed in Figs. 3(a) and 3(b), showing the time evolution and the normalized amplitude spectrum, respectively, of both the average plasma density $\bar{n}_e$ (solid black line) and the average neutral density $\bar{n}_n$ (dashed black line) in the simulation domain. Moreover, Fig. 3(c) depicts the time evolution of the discharge current I_d. The time-averaged mean values of the above magnitudes and of the beam current $I_{i\infty}$, representing the total ion current leaving the simulation domain through the free loss boundary [blue boundary in Fig. 2(a)] are listed in Table 2, featuring all of them the same dominant oscillation frequency of 11.45 kHz. This result is very close to that obtained in previous simulations,[51,70,71] and is in the 10-30 kHz range reported by experiments.[42,52,53] The average n_e to n_n and $I_{i,\infty}$ to I_d phase delays are 76.13 and 20.38 degrees, respectively.

Table 2 lists the time-averaged values of the thrust, utilization, current, divergence and production efficiencies, which are defined, respectively, as

$$\eta_{thr} = \frac{F^2}{2\dot{m}_A P_d}, \quad \eta_u = \frac{\dot{m}_{i\infty}}{\dot{m}_A}, \quad \eta_{cur} = \frac{I_{i\infty}}{I_d}, \quad \eta_{div} = \frac{P_{zi\infty}}{P_{i\infty}}, \quad \eta_{prod} = \frac{I_{i\infty}}{I_{prod}}, \tag{15}$$

where $\dot{m}_{i\infty}$ is the ion mass flow leaving the domain through the free loss boundary [blue boundary in Fig. 2(a)], F is the thrust force, obtained as the axial momentum flux of the heavy species integrated over the aforementioned boundary, $P_d = V_d I_d$ is the discharge power, $P_{zi\infty}$ and $P_{i\infty}$ are the axial and total ion power deposited to the free loss domain boundary, respectively, and $I_{prod} = I_{wi} + I_{i\infty}$ is the total ion current produced though the ionization processes, with I_{wi} the total ion current collected at the thruster walls (i.e. the anode and dielectric walls). Along with the time-averaged values of F and P_d, Table 2 also gathers the obtained specific impulse $I_sp = F/g_0\dot{m}_A$, with $g_0 = 9.80665$ ms^{-2} the standard acceleration of gravity, and the values of (i) the useful power P_{use}, invested in the thrust generation through the ions acceleration, (ii) the power spent in the ionization and excitation processes $P_{ion,ex}$ and (iii) the total power deposited by the plasma to the thruster walls (i.e. the anode and the dielectric walls) plus the electron energy flow and the heavy species non-axial energy flow through the free loss boundary P_{walls}.

The ionization instability induces peak values of the discharge current of around 6 times the mean value. These large oscillations greatly affect the whole plasma discharge and complicate its analysis, introducing uncertainties in the thruster performance figures estimates. The phase shift between the oscillating average plasma and neutral densities in the domain, partially mitigated by the ion recombination at the thruster walls, is responsible for the higher-than-expected η_u values. The temporal evolution of the thrust efficiency

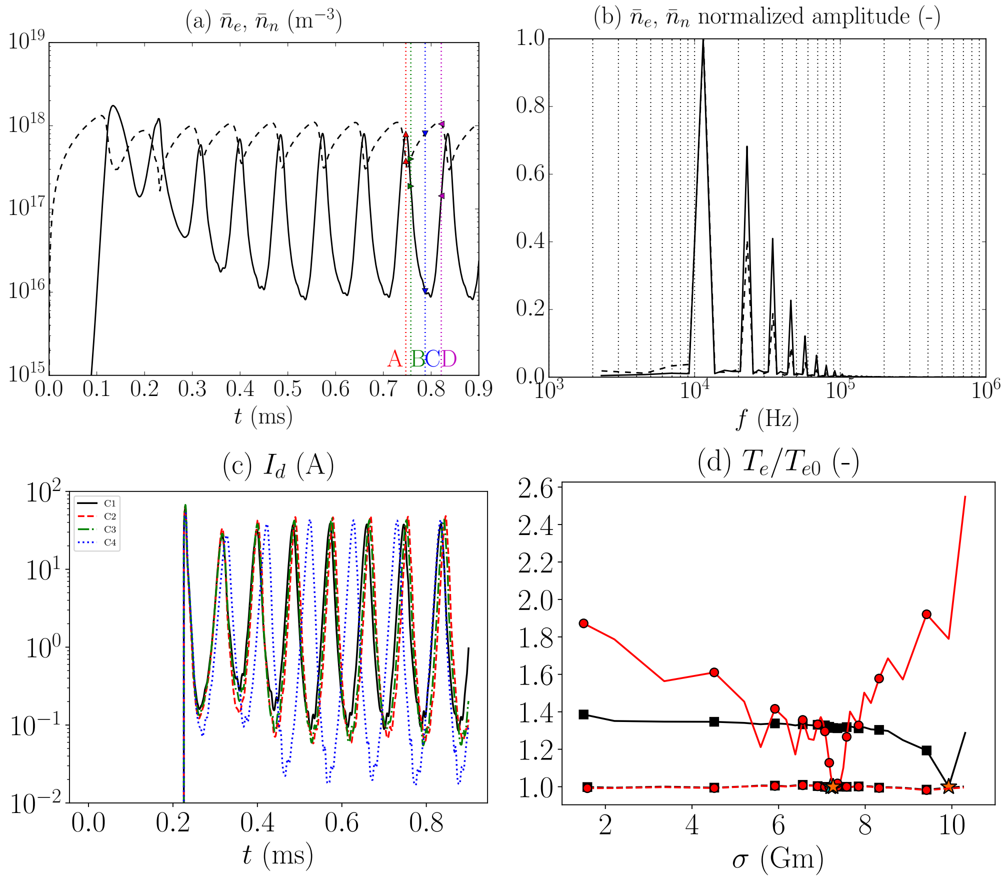

Figure 3. (a) and (b) Time evolution and normalized amplitude spectrum of $\bar{n}_e$ and $\bar{n}_n$ for the reference case, respectively. Solid and dashed lines in (a) and (b) corresponds to $\bar{n}_e$ and $\bar{n}_n$, respectively. (c) Time evolution of I_d for the simulation cases C1-C4. (d) Spatial evolution of the electron temperature ratio T_e/T_{e0} along the cathode magnetic field streamline for the cases C1 and C2. The orange star markers indicate the cathode position along the magnetic field streamline. The black and red dashed lines with square and circle markers correspond to the temperature ratio T_e/T_{e0} along the cyan magnetic line plotted in Fig. 2(b) for the cases C1 and C2, respectively. The cyan star marker indicates the reference point for T_{e0} in that line.

yields a mean value of 0.48. Given its non-linear dependence on the oscillating thrust and discharge power, a more representative value of 0.28 is obtained using the time-averaged values in Table 2, which is closer to the useful-to-discharge power ratio $P_{use}/P_d = 0.34$.

The electric potential axial profile shown in Fig. 4(a) presents its global maximum and minimum values at ∼0.3 cm away from the anode wall, and at the axial position of the cathode magnetic line, respectively. The maximum axial electric field, which characterizes the acceleration region, and the maximum electron temperature are located between the thruster chamber exit plane and the cathode magnetic line, as shown in Figs. 4(c) and 4(e), respectively. This is also evident from the 2D contour maps of the electric field magnitude and the electron temperature depicted in Figs. 6(b) and 6(c), respectively.

The plasma density profile shown in Fig. 4(g) features a maximum upstream the acceleration region, inside the thruster chamber [see the time-average 2D contour map in Fig. 6(d)], and decreases monotonically towards both the anode wall and the thruster exit plane due to the ion acceleration by the self-adjusted electric field shown in Fig. 6(b), thus yielding the ion streamlines depicted in Fig. 7(e). As expected, the same applies to the singly and doubly charged ion populations, their axial density profiles and singly-to-doubly charged ions particle density ratio n_{i1}/n_{i2} shown in Figs. 4(b), 4(d) and 4(f), respectively.

The ionization region, characterized by the maximum plasma density in the domain, is located closer to the anode wall than expected. This fact is related to the lack of an electric potential plateau along the first part of the thruster chamber [see Figs. 4(a) and 6(a)], which has been reported by experiments,[72–75] and greatly depends on the electron turbulent parameter profile simulated (see Sec. V.B.2). In the near plume region, Fig. 6(d) reveals a higher plasma density along the symmetry axis with respect to the upper free loss boundary. This fact is due to the natural particle reflection at the axis, which, as expected, increases the singly and doubly charged ions particle density along the axis (see Fig. 6(e) for the singly charged ions), thus giving rise to the formation of a single-peaked plasma plume downstream.

The progressive ionization of the injected neutral gas is responsible for the monotonically decreasing axial neutral density profile shown in Fig. 4(h). The ion-wall recombination and subsequent neutral emission from the lateral thruster walls is responsible for most of the neutral particle density in the lateral near plume regions, as shown in Fig. 6(g).

As already observed by Ahedo *et al.*,[64,65] Figs. 5(a) and 6(h) reveal a higher electron drift-to-internal energy ratio $m_e u_e^2/2T_e$ at the anode and near plume regions. This ratio is here limited to two (refer to Secs. IV and A). Therefore, larger values could arise at those regions if a less restrictive tolerance is considered, which suggests that the electron inertia could play a non-negligible role there.

Figures 5(b) and 5(c) show the axial profiles of the electron azimuthal and perpendicular current density components, which, neglecting collisions in Eq. (5), satisfy $j_{\theta e} \simeq -\chi^* j_{\top e}$. The electron current density components above feature a change of sign when crossing the cathode magnetic line. This is consistent with the negative axial component of the electric field that develops in that region [see Fig. 4(c)], which has also been reported by experiments.[72,73]

The cathode injection increases the electron parallel current density along the nearby magnetic field lines, as depicted in Fig. 5(d). The electron streamlines shown in Fig. 7(a) illustrate how the collisional processes taking place in the very near plume region yield a perpendicular electron transport towards both the thruster chamber and the free loss domain boundary. The former constitutes the back-streaming flow of primary electrons in charge of ionizing the neutral gas injected through the anode, which are highly magnetized and feature a diffusive-collisional motion characterized by the dominant azimuthal $\boldsymbol{E} \times \boldsymbol{B}$ drift,[1,3] and a reduced perpendicular motion through the anode. As shown in Fig. 4(e), they are heated up by the collisions in the region between the cathode magnetic line and the thruster chamber exit plane. Inside the chamber, the electron temperature decreases due to the neutral gas ionization and excitation processes and the wall losses. On the other hand, the later are responsible for the ion beam neutralization in the near plume region, and is favored by a potential jump of ∼25 V between the cathode and the free loss domain boundary [see Fig. 6(a)].

After describing the results for the reference case C1, the remaining of this section analyzes the effects of the cathode location on the discharge by comparing the cases C1-C4. Figure 3(c) compares the time evolution of the discharge current for the cases above. The characteristic breathing mode oscillation frequency for the cases C2 and C3 is 11.26 kHz and 11.30 kHz, respectively, thus very close the value of 11.45 kHz of the reference case C1. In contrast, the case C4 presents a lower value of 9.66 kHz and a larger peak-to-peak oscillation amplitude, with discharge current peak values around 7 times higher than the mean value. Table 2 lists the time-averaged values of ν_{cat}. The larger this value the more concentrated is the electron injection through the volumetric cathode, and thus the larger the perturbation that it induces in the rest of magnitudes. Referring to Eq. (2), ν_{cat} is inversely proportional to both the plasma density at the cathode MFAM cell and its volume V_{cat}. Therefore, considering that all cases C1-C4 feature a similar time-averaged value of I_d (see Table 2), the lower volume of the cathode MFAM cell C4 (see Table 1) and the lower value of the time-averaged plasma density in that region [refer to Fig. B.3 in Ref. 25, omitted here], could explain the larger discharge oscillations found for the case C4.

Given the near-collisionless parallel motion of the confined electron population typical of a HET, the plasma density and the electric potential may be assumed to satisfy the isothermal Boltzmann relation,[76] which, integrating Eq. (3) along the cathode magnetic line neglecting the effect of collisions (i.e. setting $j_{\|c} = 0$) and considering isothermal electrons, may be written as

$$e(\phi(\sigma) - \phi_0) - T_{e0} \ln\left(\frac{n_e(\sigma)}{n_{e0}}\right) = 0 \tag{16}$$

where the electron temperature T_{e0}, the plasma density n_{e0} and the electric potential ϕ_0 are constant along the cathode magnetic field streamline (i.e. $\lambda = const.$ line). Considering values of $T_{e0} = 6.41$ eV and $T_{e0} = 2.20$ eV at the cathode MFAM cell for the cases C1 and C2, respectively, the black and red solid lines in Fig. 3(d) represent the electron temperature ratio T_e/T_{e0} along the cathode magnetic line for cases C1 and C2 [see Fig. 2(b)]. For each case, the cathode location on the magnetic line is indicated by the orange star marker. The results reveal that in both cases the cathode magnetic line is far from being isothermal, specially near the cathode position. The intense volumetric injection of thermal electrons with temperature T_{cat} perturbs locally the plasma solution making the electron temperature tend to T_{cat} in the region near the cathode MFAM cell. Consequently, an electric potential jump along the cathode magnetic line develops in the cathode vecinity. For the case C1 it takes a value of $\sim$15 V, the isopotential lines of 5, 10 and 15 V depicted in Fig. 6(a) being perpendicular to the red cathode magnetic field streamline. Nonetheless, for both cases C1 and C2, the black and red dashed lines with square and circle markers in Fig. 3(d), respectively, show that the isothermal condition is satisfied along the magnetic field streamline represented by the cyan line in Fig. 2(b), thus confirming that the volumetric cathode perturbation is local.

As for the thruster performance figures, very similar results for thrust, specific impulse and efficiencies are obtained for the cases C1-C3. The case C4 however, features slightly higher thrust, specific impulse and thrust efficiency values (see Table 2). The fact that the cathode magnetic streamline is located further downstream in the case C4 [see Fig. 2(b)] results in a smoother electric potential evolution in the near plume region, as shown in Fig. 4(a). As a consequence, the axial component of the electric field shown in Fig. 4(c) features a lower peak value, but remains positive in a wider region until the cathode magnetic line, thus yielding a higher thrust.

Interestingly, the electron temperature follows the trend of the electric potential and a decaying profile is found for the case C4 in the near plume region, as shown in Fig. 4(e), while a very similar electron temperature peak value and evolution inside the thruster chamber is found in all cases. The still relatively high electron magnetization in the near plume region could explain the flat evolution of the electric potential and the electron temperature there. On the other hand, the electron drift-to-internal energy ratio shown in Fig. 5(a) remains one order of magnitude lower than those of the cases C1-C3 in most of the near plume region, thus indicating the marginal role of the electron inertial effects there.

The perturbation on the plasma density shown in Fig. 4(g) for the cases C1-C3, produced by the behavior of the electric field around the cathode magnetic line region, does not appear in the case C4, for which the corresponding cathode magnetic line crosses the domain further downstream. The same applies to the singly and doubly charged ions particle density and their density ratio depicted in Figs. 4(b), 4(d) and 4(f), respectively.

As aforementioned for the case C1, the azimuthal and perpendicular electron current density components exhibit a change of sign when crossing the cathode magnetic line on each case, as shown in Figs. 5(b) and 5(c), respectively, in accordance with the sign of the dominant axial component of the electric field there [see Fig. 4(c)]. For each case, the sign of the parallel electron current density component peaks depicted in Fig. 5(d) is consistent with the position of the cathode with respect to the axial line at $r = 4.63$ cm (see Fig. 7), $-j_{\parallel e}$ featuring the sign of the electron parallel drift velocity.

Figures 5(e)-(f) and 7 compares respectively, the axial profiles and the magnitude and streamlines of the time-averaged the 2D (z, r) electron and ion current densities $\tilde{\boldsymbol{j}}_e$ and $\tilde{\boldsymbol{j}}_i$ for cases C1-C4. The cathode location has a minor effect on the ion current density, while the electron streamlines evidence the different electron injection locations in the near plume. Interestingly, a similar solution is found for the electron streamlines inside the thruster chamber. The proximity of the simulation boundary to the cathode magnetic line in the case C4 [see Fig. 2(b)] could explain the larger discrepancies found for the case C4. Moreover, Fig. 7 reveals an oscillating pattern in the parallel electron current density along the magnetic lines in the vicinity of the volumetric cathode in the near plume region. This effect is most probably due to numerical issues related to the abrupt MFAM cells change of size in that region.

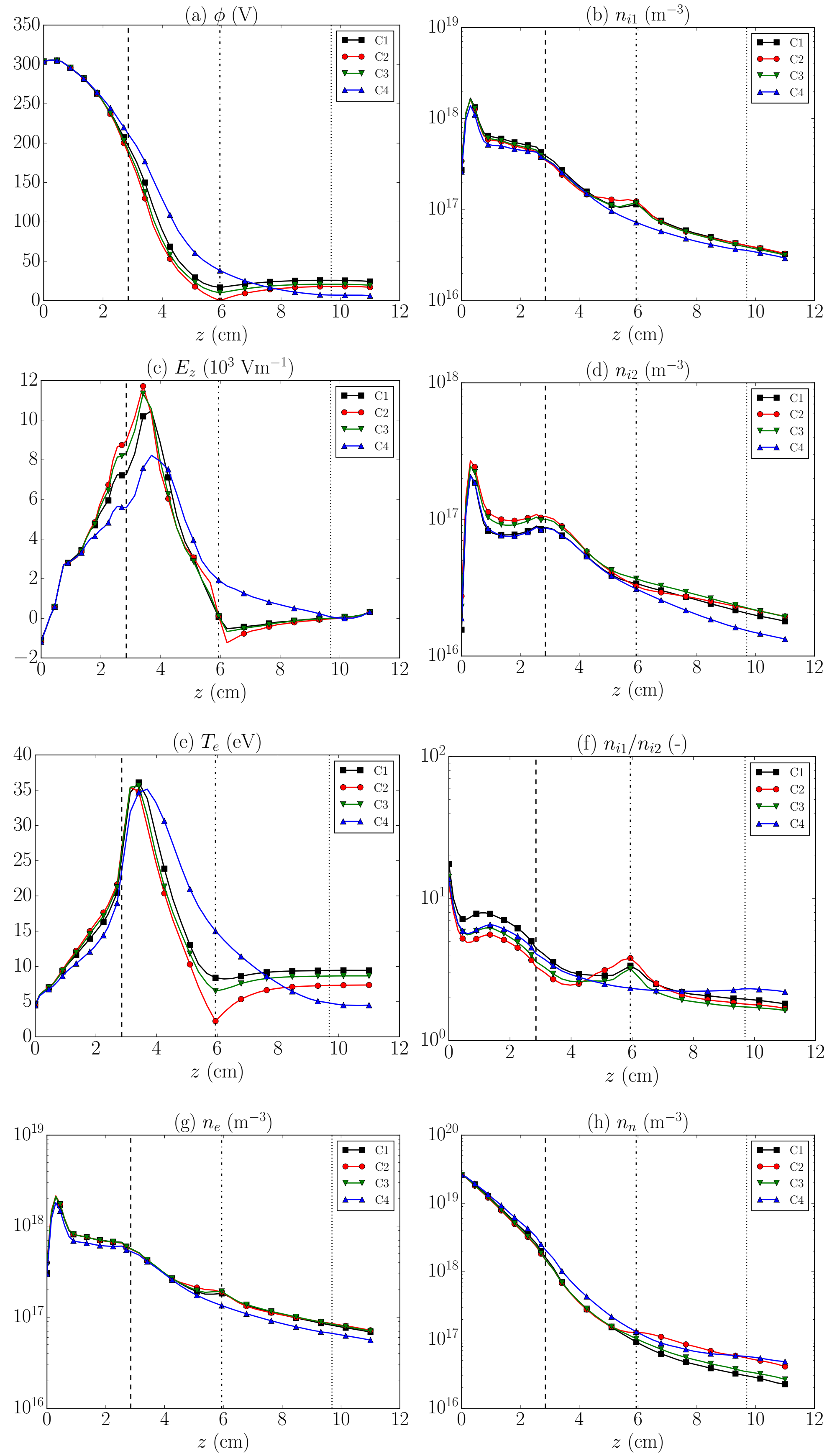

Figure 4. Time-averaged axial profiles for cases C1-C4. (a) The electric potential, (b) and (d) the singly and doubly charged ions particle density, (c) the axial component of the electric field, (e) the electron temperature, (f) the singly-to-doubly charged ions particle density ratio, and (g) and (h) the plasma and neutral density.

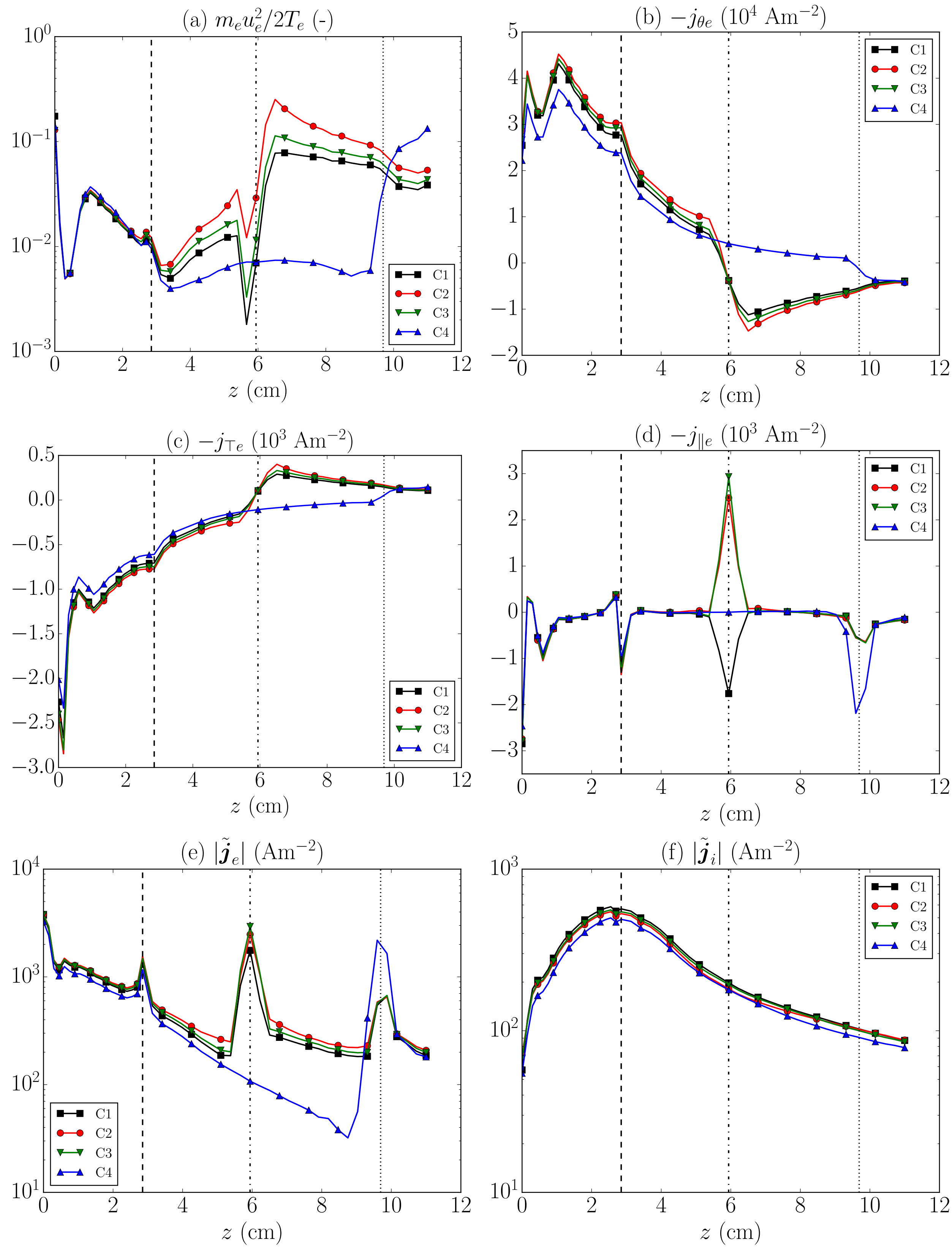

Figure 5. Time-averaged axial profiles for cases C1-C4. (a) The electron drift-to-internal energy ratio, (b) the electron azimuthal current density component, (c) the electron perpendicular current density component, (d) the electron parallel current density component, (e) the magnitude of the 2D (z, r) electron current density vector and (f) the magnitude of the 2D (z, r) ion current density vector.

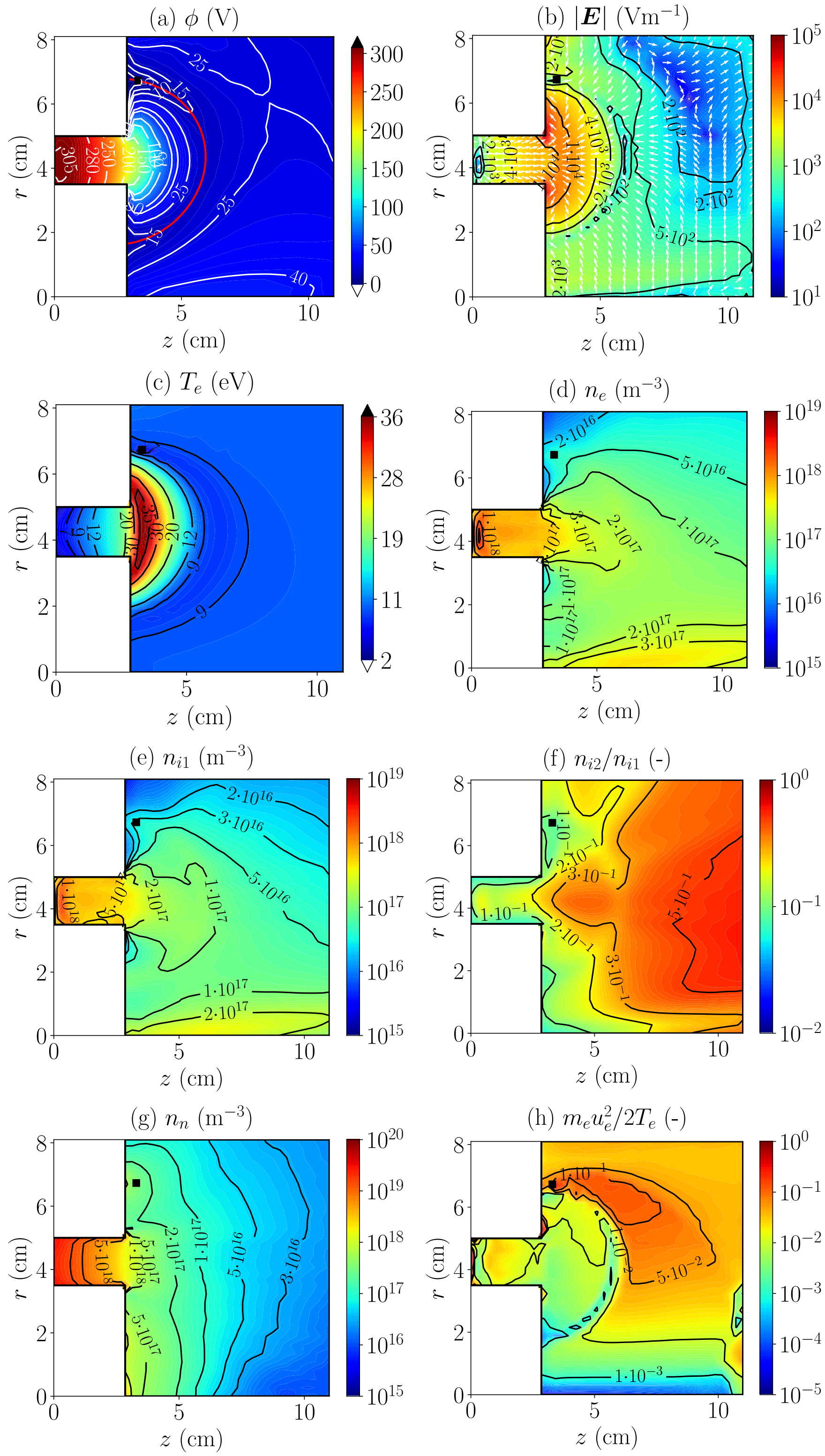

Figure 6. Case C1 time-averaged 2D contour maps of (a) the electric potential, (b) the electric field magnitude, (c) the electron temperature, (d) the plasma density, (e) the singly charged ions particle density, (f) the doubly-to-singly charged ions particle density ratio, (g) the neutrals particle density and (h) the electron drift-to-internal energy ratio. The black square marker indicates the cathode position for the case C1. In (a) the red line represents the magnetic field streamline passing through the cathode. In (b) the white arrows show the direction of the electric field.

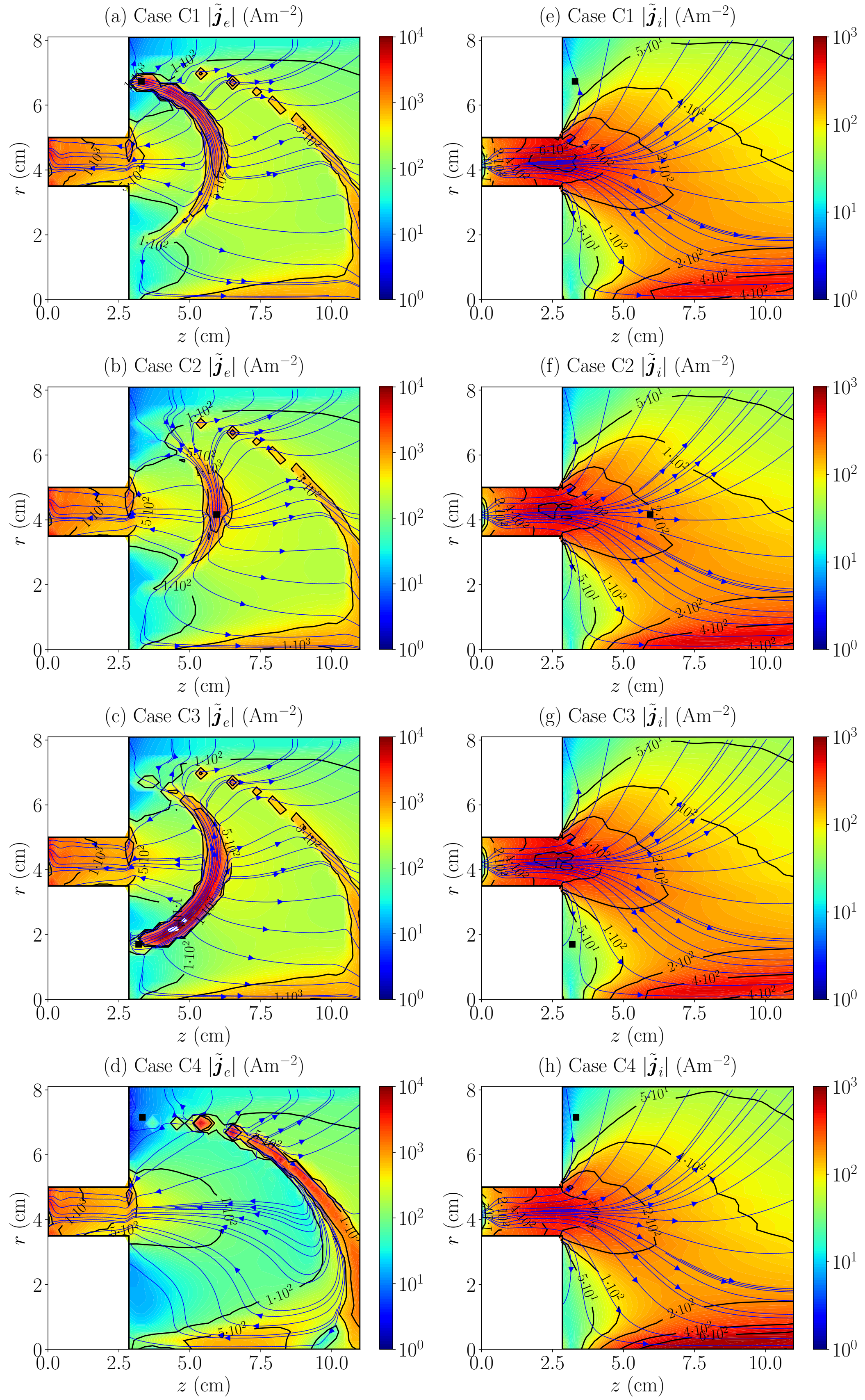

Figure 7. 2D magnitude contour plots and streamlines of the time-averaged electron (a)-(d) and ion (e)-(h) 2D (z, r) current density vectors $-\tilde{j}_e$ and $\tilde{j}_i$, respectively, for cases C1-C4. The black square marker indicates the cathode position for each case.

2. Results for various electron turbulent transport parameter profiles

Table 3 defines the simulation cases considered in this section featuring various α_t profiles. The rest of simulation parameters are kept constant to those of the reference case described in Sec. V.A, which shall be here referred to as T1. The case T2 features a constant α_t profile with twice the value of the reference case T1. On the other hand, various step-out profiles have been considered following two trends: cases T3-T5 increase the turbulent contribution in the near plume region while keeping it constant inside the thruster chamber; cases T5-T7 decrease the turbulent contribution inside the thruster chamber while keeping it constant in the near plume region. The main simulation results and relevant aspects of all the cases above are commented in this section along with Figs. 8-10. In order to facilitate the analysis, the results are here presented in two groups, named G1 and G2. The former refers to the cases T1-T5, and the latter gathers the cases T1 and T5-T7. Figures 8(a) and 9, and 8(b) and 10 show the results for G1 and G2, respectively. The vertical black dashed and dot-dashed lines in Figs. 9 and 10 indicate, respectively, the axial position of the thruster chamber exit plane at $z = 2.85$ cm and the axial position of the magnetic field streamline passing through the cathode at $z = 5.94$ cm. Additionally, Table 4 lists the relevant discharge data for the cases T2-T7.

Case	**Turbulent parameter profile type**
T1	Constant profile with $\alpha_t = 2.5\%$
T2	Constant profile with $\alpha_t = 5.0\%$
T3	Step-out profile at $z = 2.85$ cm with $\alpha_t = 2.5 - 5.0\%$
T4	Step-out profile at $z = 2.85$ cm with $\alpha_t = 2.5 - 7.5\%$
T5	Step-out profile at $z = 2.85$ cm with $\alpha_t = 2.5 - 10.0\%$
T6	Step-out profile at $z = 2.85$ cm with $\alpha_t = 2.0 - 10.0\%$
T7	Step-out profile at $z = 2.85$ cm with $\alpha_t = 1.5 - 10.0\%$

Table 3. Definition of the simulation cases T1-T7 featuring different turbulent parameter profiles. The values of the turbulent parameter α_t refer to the percentage of the electron electron cyclotron frequency ω_{ce} corresponding to the equivalent electron turbulent collision frequency. The axial location of the α_t step is at the thruster chamber exit plane. The hyphen separates the α_t values inside the thruster chamber and in the near plume region.

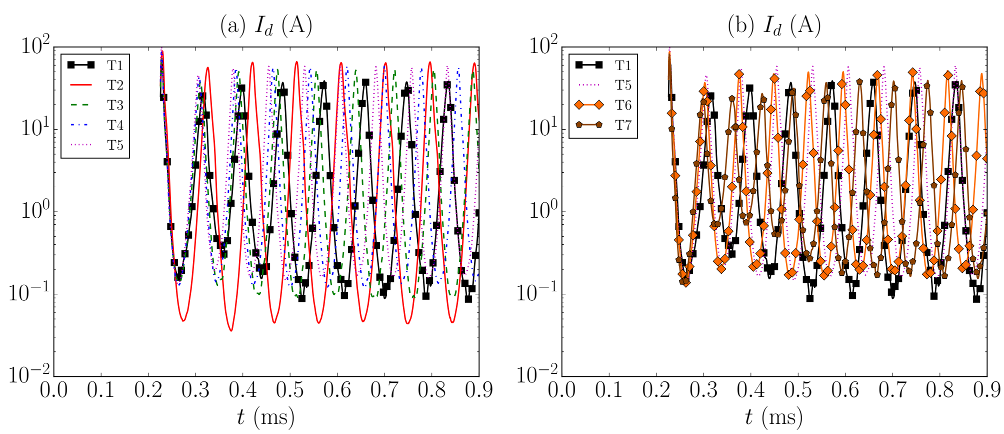

Figure 8. Time evolution of I_d for G1 (a) and G2 (b).

Figs. 8(a) and 8(b) show the time evolution of the discharge current for G1 and G2, respectively. As commented in Sec. V.B.1, the results highlight the need for a control strategy for the discharge current in order to obtain time-averaged values closer to those reported by experiments.[68] The largest peak values are obtained for the case T2, which also features the lowest breathing mode frequency of 10.65 kHz. Increasing α_t in the near plume region yields a higher breathing mode frequency, which takes the values of 12.12, 12.74 and 13.20 kHz for the cases T3-T5, respectively. A similar effect is found when reducing α_t in the thruster chamber, the breathing mode frequency being 13.61 and 14.04 kHz for the cases T6 and T7, respectively.

From Figs. 9(a) and 10(a) it is clear that the larger the α_t value inside the thruster chamber, the

Variable	Units	T2	T3	T4	T5	T6	T7
$\bar{n}_e$	10^{17} m^{-3}	1.70	1.59	1.64	1.63	1.59	1.50
$\bar{n}_n$	10^{17} m^{-3}	7.13	6.46	6.09	5.80	5.85	5.97
I_d	A	9.40	1.59	7.79	8.08	7.24	6.33
$I_{i\infty}$	A	5.41	6.46	5.53	5.28	5.14	4.91
η_{thr}	-	0.23	0.28	0.27	0.27	0.29	0.33
η_u	-	0.97	0.98	0.99	0.98	0.98	0.98
η_{cur}	-	0.58	0.71	0.68	0.65	0.71	0.78
η_{div}	-	0.75	0.83	0.82	0.83	0.82	0.85
η_{prod}	-	0.56	0.60	0.60	0.57	0.59	0.61
I_{sp}	s	1636	1597	1615	1658	1626	1609
F	mN	80.24	78.09	79.16	81.07	79.18	78.84
P_d	W	2821	2205	2337	2425	2172	1899
P_{use}	W	774	728	754	792	752	745
P_{walls}	W	1663	1197	1347	1430	1256	1002
$P_{ion,ex}$	W	225	188	197	185	163	151

Table 4. Main results for the simulation cases T2-T7. Time-averaged values over the number of complete cycles within the last 450 μs of simulation time.

flatter the electric potential profile in the first part of the chamber. This behavior has been observed in experiments.[74] According to previous stationary plasma thruster simulations,[5,77] a larger axial potential fall is found within the thruster chamber for both increasing α_t in the near plume region (i.e. the cases T3-T5, respectively), and decreasing α_t inside the thruster chamber (i.e. the cases T5-T7, respectively). As shown in Figs. 9(c) and 10(c), the peak in the axial component of the electric field increases accordingly, and moves upstream into the thruster chamber for all the step-out cases T3-T7, presenting the case T7 the maximum E_z peak value. According to Fig. 9(e), the electron temperature peak increases for higher values of α_t in the near plume region due to the enhanced Joule heating there [the higher electron effective collisionality in the near plume region for cases T3-T5 yields lower values of the effective Hall parameter, as shown in Fig. 9(b)]. In contrast, it decreases and moves upstream into the thruster chamber when decreasing the turbulent contribution inside the chamber, as depicted in Fig. 10(e). The obtained electron temperature peak values are not far from those reported by experiments,[72–75] the case T2 presenting the larger discrepancies with respect to the rest of the cases here analyzed.

The behavior of the effective Hall parameter is clearly dominated by the electron turbulent contribution in all cases, as shown in Figs. 9(b) and 10(b). Figure 9(d) depicts a lower magnitude of $j_{\theta e}$ along the near plume region in the cases T3-T5. This is consistent with the lower magnetization of the electron population due the higher electron effective collisionality in that region [see the corresponding values of the effective Hall parameter in Fig. 9(b)]. Consequently, the higher electron magnetization inside the thruster chamber in the cases T5-T7 yields larger $j_{\theta e}$ values there, as shown in Fig. 10(d), and reduces the electron perpendicular transport towards the anode, as can be seen in Fig. 10(f). This is in line with the decreasing trend of the time-averaged discharge current values listed in Table 4 for the cases T5-T7, respectively.

Finally, as shown in Table 4, the thrust efficiency increases for lower values of the electron turbulent contribution inside the thruster chamber (i.e. the cases T5-T7). Since all cases here feature both a constant discharge voltage and propellant mass flow, this fact is due to the significant decrease in the time-averaged discharge current from the case T5 to T7, commented above. On the other hand, the thrust efficiency is not significantly affected when increasing α_t in the near plume region.

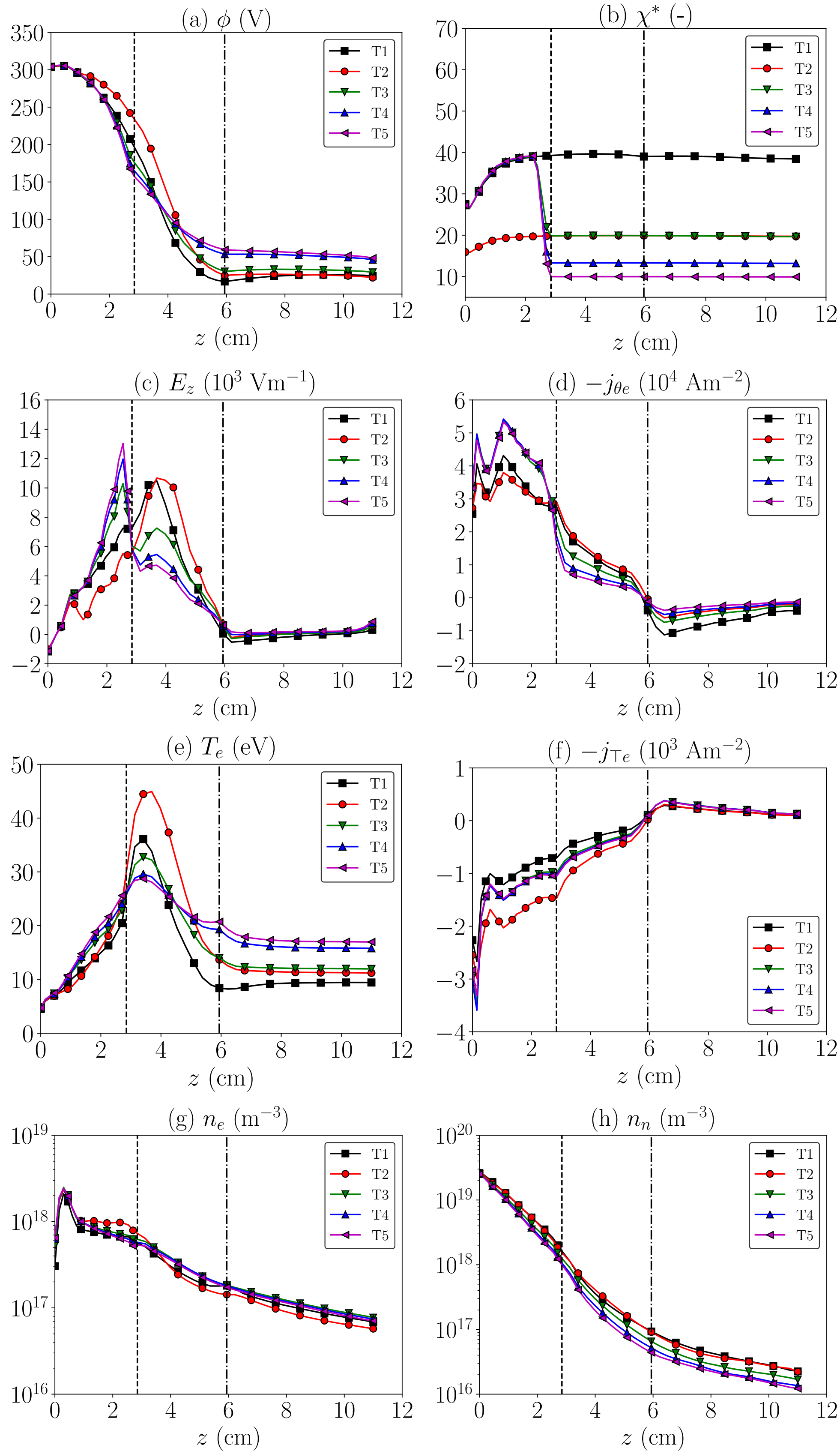

Figure 9. Time-averaged axial profiles for G1 of (a) the electric potential, (b) the effective Hall parameter, (c) the axial component of the electric field, the electron azimuthal (d) and perpendicular (f) current density components, (e) the electron temperature, and the plasma (g) and neutrals (h) particle density.

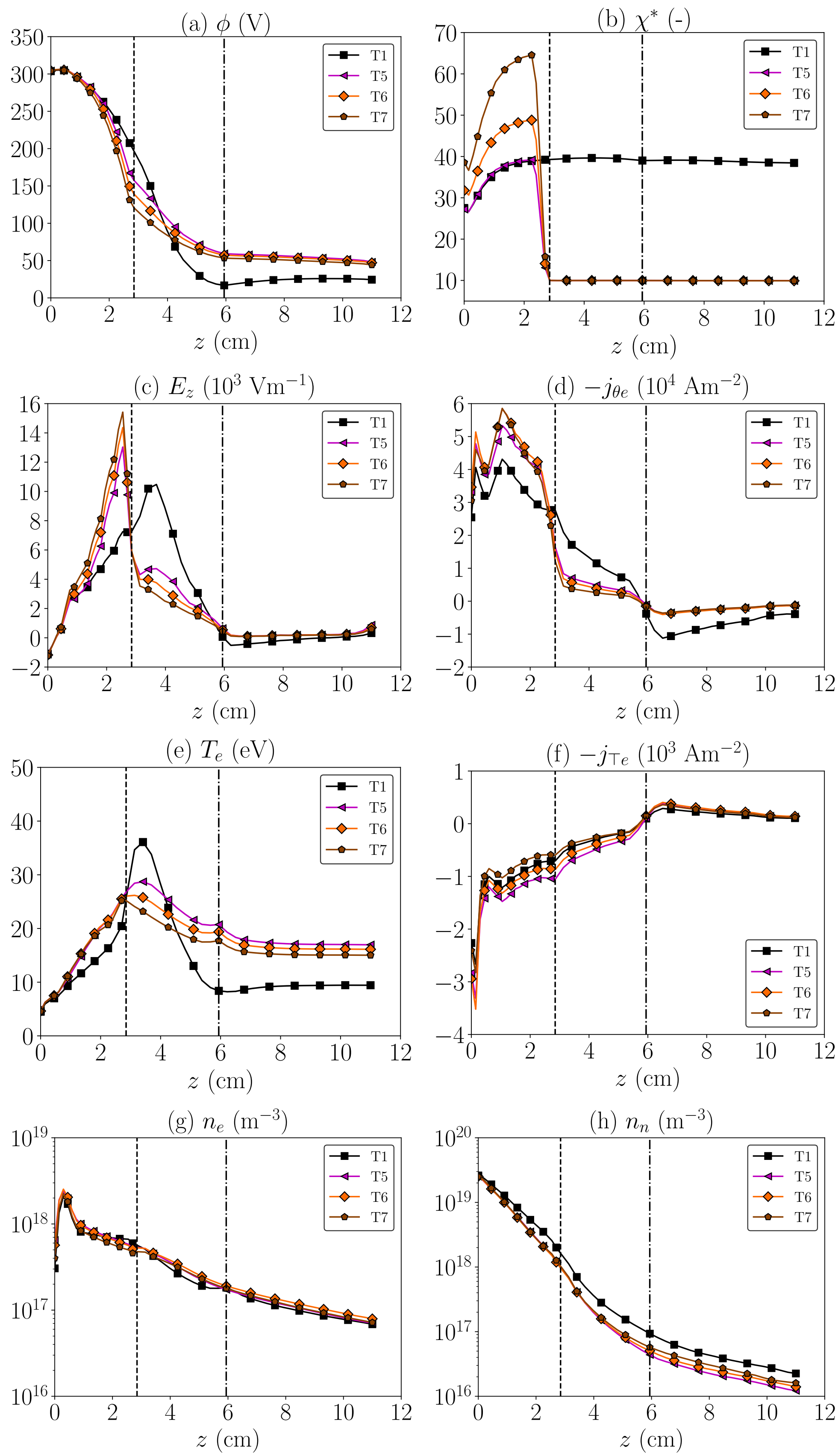

Figure 10. Time-averaged axial profiles for G2 of (a) the electric potential, (b) the effective Hall parameter, (c) the axial component of the electric field, the electron azimuthal (d) and perpendicular (f) current density components, (e) the electron temperature, and the plasma (g) and neutrals (h) particle density.

C. Conclusions

This work has permitted to evaluate the HYPHEN performance through the simulation of a typical SPT-100 HET scenario, where different studies have been performed. First, a reference simulation case has been analyzed in detail. Second, the effects on the plasma discharge of the cathode location in the near plume region have been explored. Finally, a parametric study for different constant and step-out electron turbulent parameter profiles has been conducted. For all these cases contours and 1D profiles of plasma variables and mean values of thruster performances are assessed.

The well-known HET breathing mode in the 10-30 kHz range is reproduced in all simulated cases. The low frequency ionization instability induces higher-than-expected oscillations of the discharge current, with peak values ∼6-7 times the mean value under constant discharge voltage operation, which affect the whole plasma discharge and complicate the analysis introducing uncertainties in the thruster performance figures estimates. Even though these large oscillations complicates the discharge analysis and affect the thruster performance figures, the latter are not too far from those reported by experiments.[68]

The simulations reveal that the thermal injection performed within the bulk plasma breaks the usual isopotential (and isothermal) condition of the magnetic lines near the cathode region. However, this perturbation is restricted to a local region close to the cathode location, and its impact on the thruster performance figures is mild. Similar plasma profiles inside the thruster chamber and thruster performance figures are obtained when moving the cathode position along the same magnetic field streamline (cases C1-C3). In contrast, smoother axial profiles of the electric potential and the electron temperature along the near plume region are found when the cathode is placed at a larger radius (C4), so that the cathode magnetic line crosses the simulation domain further downstream.

Although the trends in the electric potential and electron temperature profiles are not too far from the behavior reported by experiments, a strategy to limit the breathing mode induced discharge oscillations is required for a finer tuning of the electron turbulent parameters.

Several actions and studies are proposed for future work. First, the aforementioned large oscillations found on the discharge current reveals the need for a future implementation of effective current control strategies such as resistor-inductor-capacitor (RLC) networks or proportional-integral-derivative (PID) control algorithms,[78,79] so that the discharge voltage V_d is not directly applied between the anode and cathode. This will allow to obtain more reliable estimates of the thruster performance figures, and will facilitate the tuning of the electron turbulent parameters aiming to better reproduce the reported experimental results.

Second, it should be discussed if the local perturbation on the plasma solution induced by the volumetric cathode is artificial or not. In this line, the extension of the volumetric cathode to several MFAM cells should be explored. Moreover, 2D-3D comparisons of the HET near plume region simulation results[80] might help justify the validity of the axisymmetric volumetric cathode model. Furthermore, the implementation of the wall cathode model presented in Ref. 81, which includes a sheath model for high emission electrodes that adjusts the electric potential there to the conditions imposed by the external plasma[82] could provide more realistic results in the near cathode region.

Third, simulation domains featuring an extended near plume region will be considered in the future to analyze the evolution of the plasma properties when the magnetic field becomes residual, and assess the effects on the plasma discharge of the boundary conditions downstream. In this line, the improved techniques proposed in Ref. 27 for the determination of the electric potential and the electron temperature at the simulation domain boundary will be incorporated.

Fourth, the development of improved simulation domain MFAMs featuring a smoother and progressive evolution of the cells size should also be tackled, and special attention should be put to the PIC-mesh-to-MFAM cell size ratio, since important interpolation errors may be present whenever this ratio significantly deviates from unity. This issue can be specially critical at the domain boundary.

Finally, the simulation of more complex magnetic topologies featuring singular points or magnetic shielding of the thruster walls, and dedicated parametric studies for different combinations of the turbulent parameters introduced in Sec. IV will be performed in the future.

VI. Acknowledgements

This work has been supported by the CHEOPS project, funded by the European Union's Horizon 2020 Research and Innovation Programme, under Grant Agreement 730135. Additional funding for A. Domínguez-Vázquez came from Project ESP2016-75887 (Spain's National Research and Development Plan - MINECO/

FEDER). The authors thank D. Pérez-Grande for his assistance with the obtention of the simulation results.

References

[1]R. G. Jahn. *Physics of electric propulsion.* McGraw-Hill, New York, 1968. Reprinted by Dover.

[2]M. Martínez-Sánchez and J. E. Pollard. Spacecraft electric propulsion-an overview. *Journal of propulsion and power*, 14(5):688–699, 1998.

[3]D. M. Goebel and I. Katz. *Fundamentals of electric propulsion: Ion and Hall thrusters.* Willey, New York, 2008.

[4]E. Ahedo. Plasmas for space propulsion. *Plasma Physics and Controlled Fusion*, 53(12):124037, 2011.

[5]J. P. Boeuf. Tutorial: physics and modeling of Hall thrusters. *Journal of Applied Physics*, 121(1):011101, 2017.

[6]F. F. Chen. Plasma ionization by helicon waves. *Plasma Physics and Controlled Fusion*, 33(4):339, 1991.

[7]R. W. Boswell and F. F. Chen. Helicons-the early years. *IEEE Transactions on Plasma Science*, 25(6):1229–1244, 1997.

[8]K. Takahashi, C. Charles, R. W. Boswell, W. Cox, and R. Hatakeyama. Transport of energetic electrons in a magnetically expanding helicon double layer plasma. *Applied Physics Letters*, 94(19):191503, 2009.

[9]E. Ahedo and J. Navarro-Cavallé. Helicon thruster plasma modeling: Two-dimensional fluid-dynamics and propulsive performances. *Physics of Plasmas*, 20(4):043512, 2013.

[10]T. Lafleur. Helicon plasma thruster discharge model. *Physics of Plasmas*, 21(4):043507, 2014.

[11]J. Navarro-Cavallé. *Plasma simulation in space propulsion: the Helicon plasma thruster.* PhD thesis, Universidad Politécnica de Madrid. Escuela Técnica Superior de Ingenieros Aeronáuticos. Departamento de Matemática Aplicada a la Ingeniería Aeroespacial, Madrid, Spain, December 2016.

[12]J Navarro-Cavallé, M Wijnen, P Fajardo, and E Ahedo. Experimental characterization of a 1 kW helicon plasma thruster. *Vacuum*, 149:69–73, 2018.

[13]B. Tian, M. Merino, and E. Ahedo. Two-dimensional plasma-wave interaction in an helicon plasma thruster with magnetic nozzle. *Plasma Sources Science and Technology*, 27(11):114003, 2018.

[14]D. B. Miller and G. W. Bethke. Cyclotron resonance thruster design techniques. *AIAA Journal*, 4(5):835–840, 1966.

[15]J. C. Sercel and D. J. Fitzgerald. ECR plasma thruster research: Preliminary theory and experiments. In *25th Joint Propulsion Conference and Exhibit*, paper AIAA 1989-2379, Monterey, CA, USA, July 10-13, 1989. American Institute of Aeronautics and Astronautics, https://www.aiaa.org.

[16]M. Lampe, G. Joyce, W. M. Manheimer, and S. P. Slinker. Quasi-neutral particle simulation of magnetized plasma discharges: General formalism and application to ECR discharges. *IEEE Transactions On Plasma Science*, 26:1592–1609, 1998.

[17]H. Kuninaka and S. Satori. Development and demonstration of a cathodeless electron cyclotron resonance ion thruster. *Journal of Propulsion and Power*, 14(6):1022–1026, 1998.

[18]J. Jarrige, P. Q. Elias, F. Cannat, and D. Packan. Performance comparison of an ECR plasma thruster using argon and xenon as propellant gas. In *33rd International Electric Propulsion Conference*, paper IEPC 2013-420, Washington D. C., USA, October 7-10, 2013. Electric Rocket Propulsion Society, https://erps.spacegrant.org.

[19]T. Vialis, J. Jarrige, A. Aanesland, and D. Packan. Direct thrust measurement of an electron cyclotron resonance plasma thruster. *Journal of Propulsion and Power*, 34(5):1323–1333, 2018.

[20]F. Taccogna and L. Garrigues. Latest progress in Hall thrusters plasma modelling. *Reviews of Modern Plasma Physics*, 3(1):12, 2019.

[21]H. Kentaro. An overview of discharge plasma modeling for Hall effect thrusters. *Plasma Sources Science and Technology*, 28(4):044001, 2019.

[22]J. M. Fife. *Hybrid-PIC modeling and electrostatic probe survey of Hall thrusters.* PhD thesis, Aeronautics and Astronautics Dept., Massachuchusetts Institute of Technology, Cambridge, Massachusetts, USA, September 1998.

[23]F. I. Parra, E. Ahedo, J. M. Fife, and M. Martínez-Sánchez. A two-dimensional hybrid model of the Hall thruster discharge. *Journal of Applied Physics*, 100(2):023304, 2006.

[24]D. Escobar and E. Ahedo. Two-dimensional electron model for a hybrid code of a two-stage Hall thruster. *IEEE Transactions on Plasma Science*, 36(0):2043–2057, 2008.

[25]A. Domínguez-Vázquez. *Axisymmetric simulation codes for Hall effect thrusters and plasma plumes.* PhD thesis, Universidad Carlos III de Madrid (UC3M), Leganés, Madrid, Spain. To be defended in 2019.

[26]J. Zhou, A. Domínguez-Vázquez, D. Pérez-Grande, P. Fajardo, and E. Ahedo. An axisymmetric hybrid model for the plasma transport in a Helicon plasma thruster. In *Space Propulsion Conference*, paper SP2018-308, Sevilla, Spain, May 14-18, 2018. 3AF, https://www.3af.fr/.

[27]J. Zhou, D. Pérez-Grande, P. Fajardo, and E. Ahedo. Numerical treatment of a magnetized electron fluid within an electromagnetic plasma thruster code. Submitted to PSST.

[28]J. Zhou, P. Jiménez, M. Merino, P. Fajardo, and E. Ahedo. Numerical simulations of the plasma discharge in an helicon plasma thruster. In *36th International Electric Propulsion Conference*, paper IEPC 2019-330, Vienna, Austria, 2019. Electric Rocket Propulsion Society, https://erps.spacegrant.org.

[29]A. Sánchez-Villar and M. Merino. Advances in wave-plasma modelling in ECR thrusters. In *Space Propulsion Conference*, paper SP2018-346, Sevilla, Spain, May 14-18, 2018. 3AF, https://www.3af.fr/.

[30]A. Sánchez-Villar, J. Zhou, M. Merino, P. Fajardo, and E. Ahedo. PIC/fluid/wave simulations of the plasma discharge in an ECR plasma thruster. In *36th International Electric Propulsion Conference*, paper IEPC 2019-633, Vienna, Austria, 2019. Electric Rocket Propulsion Society, https://erps.spacegrant.org.

[31]A. Domínguez-Vázquez, D. Pérez-Grande, P. Fajardo, and E. Ahedo. NOMADS: development of a versatile plasma discharge simulation platform for electric propulsion. In *Space Propulsion Conference*, paper SP2016-3124869, Rome, Italy, May 2-6, 2016. 3AF, https://www.3af.fr/.

[32] A. Domínguez-Vázquez, F. Cichocki, M. Merino, P. Fajardo, and E. Ahedo. 2D and 3D hybrid PIC-fluid modeling of electric thruster plumes. In *35th International Electric Propulsion Conference*, paper IEPC 2017-209, Atlanta, GA, USA, October 8-12, 2017. Electric Rocket Propulsion Society, https://erps.spacegrant.org.

[33] A. Domínguez-Vázquez, F. Cichocki, M. Merino, P. Fajardo, and E. Ahedo. Axisymmetric plasma plume characterization with 2D and 3D particle codes. *Plasma Sources Science and Technology*, 27(10):104009, 2018.

[34] R. R. Hofer, B. A. Jorns, J. E. Polk, I. G. Mikellides, and J. S. Snyder. Wear test of a magnetically shielded Hall thruster at 3000 seconds specific impulse. In *33rd International Electric Propulsion Conference*, paper IEPC 2013-033, Washington D. C., USA, October 7-10, 2013. Electric Rocket Propulsion Society, https://erps.spacegrant.org.

[35] I. G. Mikellides, I. Katz, R. R. Hofer, and D. M. Goebel. Magnetic shielding of a laboratory Hall thruster. I. Theory and validation. *Journal of Applied Physics*, 115(4):043303, 2014.

[36] R. R. Hofer, D. M. Goebel, I. G. Mikellides, and I. Katz. Magnetic shielding of a laboratory Hall thruster. II. Experiments. *Journal of Applied Physics*, 115(4):043304, 2014.

[37] T. Andreussi, V. Giannetti, A. Leporini, M. M. Saravia, and M. Andrenucci. Influence of the magnetic field configuration on the plasma flow in Hall thrusters. *Plasma Physics and Controlled Fusion*, 60(1):014015, 2017.

[38] F. Cichocki. *Analysis of the expansion of a plasma thruster plume into vacuum*. PhD thesis, Universidad Carlos III de Madrid (UC3M), Leganés, Madrid, Spain, 2017.

[39] D. Pérez-Grande, J. Zhou, A. Domínguez-Vázquez, P. Fajardo, and E. Ahedo. Development updates for a two-dimensional axisymmetric hybrid code for plasma thruster discharges. In *35th International Electric Propulsion Conference*, paper IEPC 2017-201, Atlanta, GA, USA, October 8-12, 2017. Electric Rocket Propulsion Society, https://erps.spacegrant.org.

[40] D. Pérez-Grande. *Fluid modeling and simulation of the electron population in Hall effect thrusters with complex magnetic topologies*. PhD thesis, Universidad Carlos III de Madrid (UC3M), Leganés, Madrid, Spain, 2018.

[41] I. Maqueda, D. Escobar, and E. Ahedo. Advances on a Hall thruster hybrid code. In *30th International Electric Propulsion Conference*, paper IEPC 2007-066, Florence, Italy, September 17-20, 2007. Electric Rocket Propulsion Society, https://erps.spacegrant.org.

[42] J. P. Boeuf and L. Garrigues. Low frequency oscillations in a stationary plasma thruster. *Journal of Applied Physics*, 84(7):3541–3554, 1998.

[43] B. A. Jorns. Data driven model for electron transport in a Hall effect thruster. In *Space Propulsion Conference*, paper SP2018-346, Sevilla, Spain, May 14-18, 2018. 3AF, https://www.3af.fr/.

[44] I. G. Mikellides and A. L. Ortega. Challenges in the development and verification of first-principles models in Hall-effect thruster simulations that are based on anomalous resistivity and generalized Ohm's law. *Plasma Sources Science and Technology*, 28(1):014003, 2019.

[45] L. Garrigues, S. Santhosh, L. Grimaud, and S. Mazouffre. Operation of a low-power Hall thruster: Comparison between magnetically unshielded and shielded configuration. *Plasma Sources Science and Technology*, 28(3):034003, 2019.

[46] T. Lafleur, S. D. Baalrud, and P. Chabert. Theory for the anomalous electron transport in Hall effect thrusters. I. insights from particle-in-cell simulations. *Physics of Plasmas*, 23(5):053502, 2016.

[47] T. Lafleur, S. D. Baalrud, and P. Chabert. Theory for the anomalous electron transport in Hall effect thrusters. II. kinetic model. *Physics of Plasmas*, 23(5):053503, 2016.

[48] V. Croes, T. Lafleur, Z. Bonaventura, A. Bourdon, and P. Chabert. 2D particle-in-cell simulations of the electron drift instability and associated anomalous electron transport in Hall-effect thrusters. *Plasma Source Science and Technology*, 26(3):034001, 2017.

[49] T. Lafleur, S. D. Baalrud, and P. Chabert. Characteristics and transport effects of the electron drift instability in Hall-effect thrusters. *Plasma Sources Science and Technology*, 26(2):024008, 2017.

[50] T. Lafleur, R. Martorelli, P. Chabert, and A. Bourdon. Anomalous electron transport in Hall-effect thrusters: Comparison between quasi-linear kinetic theory and particle-in-cell simulations. *Physics of Plasmas*, 25(6):061202, 2018.

[51] J. M. Fife, M. Martínez-Sánchez, and J. Szabo. A numerical study of low-frequency discharge oscillations in Hall thrusters. In *33rd Joint Propulsion Conference and Exhibit*, paper AIAA 1997-3052, Seattle, WA, USA, July 6-9, 1997. American Institute of Aeronautics and Astronautics, https://www.aiaa.org.

[52] E. Y. Choueiri. Plasma oscillations in Hall thrusters. *Physics of Plasmas*, 8(4):1411–1426, 2001.

[53] S. Barral and E. Ahedo. Low-frequency model of breathing oscillations in Hall discharges. *Physical Review E*, 79(4):046401, 2009.

[54] R. Santos. *Código híbrido avanzado de motores de plasma de efecto Hall*. PhD thesis, Universidad Politécnica de Madrid. Escuela Técnica Superior de Ingenieros Aeronáuticos. Departamento de Fundamentos Matemáticos, Madrid, Spain, Junio 2012.

[55] D. Escobar. *Electron transport and azimuthal oscillations in Hall thrusters*. PhD thesis, Universidad Politécnica de Madrid. Escuela Técnica Superior de Ingenieros Aeronáuticos. Departamento de Fundamentos Matemáticos, Madrid, Spain, June 2015.

[56] F. Cichocki, A. Domínguez, M. Merino, and E. Ahedo. A 3D hybrid code to study electric thruster plumes. In *Space Propulsion Conference*, paper SP2016-3124968, Rome, Italy, May 2-6, 2016. 3AF, https://www.3af.fr/.

[57] F. Cichocki, A. Domínguez-Vázquez, M. Merino, and E. Ahedo. Hybrid 3D model for the interaction of plasma thruster plumes with nearby objects. *Plasma Sources Science and Technology*, 26(12):125008, 2017.

[58] F. Cichocki, M. Merino, and E. Ahedo. A 3d electron fluid model to study magnetic field effects on an expanding plasma thruster plume. In *Space Propulsion Conference*, paper SP2018-295, Sevilla, Spain, May 14-18, 2018. 3AF, https://www.3af.fr/.

[59] M. Mitchner and C. H. Kruger Jr., editors. *Partially ionized gases*. John Wiley and Sons, Inc., New York, 1973.

[60] E. W. Bell, N. Djurić, and G. H. Dunn. Electron-impact ionization of In^+ and Xe^+. *Physical Review A*, 48(6):4286, 1993.

[61] D. Pérez-Grande, O. Gonzalez-Martinez, P. Fajardo, and E. Ahedo. Analysis of the numerical diffusion in anisotropic mediums: Benchmarks for magnetic field aligned meshes in space propulsion simulations. *Applied Sciences*, 6(11):354, 2016.

[62]E. Sozer, C. Brehm, and C. C. Kiris. Gradient calculation methods on arbitrary polyhedral unstructured meshes for cell-centered CFD solvers. In *52nd AIAA Aerospace Sciences Meeting*, paper AIAA 2014-1440, National Harbor, MD, USA, January 13-17, 2014. American Institute of Aeronautics and Astronautics, https://www.aiaa.org.

[63]E. Ahedo and V. de Pablo. Combined effects of electron partial thermalization and secondary emission in Hall thruster discharges. *Physics of Plasmas*, 14:083501, 2007.

[64]E. Ahedo, J. M. Gallardo, and M. Martınez-Sánchez. Model of the plasma discharge in a Hall thruster with heat conduction. *Physics of Plasmas*, 9(9):4061–4070, 2002.

[65]E Ahedo and J Rus. Vanishing of the negative anode sheath in a Hall thruster. *Journal of Applied Physics*, 98(4):043306, 2005.

[66]C. G. Petra, O. Schenk, M. Lubin, and K. Gäertner. An augmented incomplete factorization approach for computing the Schur complement in stochastic optimization. *SIAM Journal on Scientific Computing*, 36(2):C139–C162, 2014.

[67]C. G. Petra, O. Schenk, and M. Anitescu. Real-time stochastic optimization of complex energy systems on high-performance computers. *Computing in Science & Engineering*, 16(5):32–42, 2014.

[68]J. R. Brophy. Stationary plasma thruster evaluation in Russia. 1992.

[69]V.J. Murray, M.D. Pilinski, E.J. Smoll Jr, M. Qian, T.K. Minton, S.M. Madzunkov, and M.R. Darrach. Gas–surface scattering dynamics applied to concentration of gases for mass spectrometry in tenuous atmospheres. *The Journal of Physical Chemistry C*, 121(14):7903–7922, 2017.

[70]M. K. Scharfe, N. Gascon, M. A. Cappelli, and E. Fernández. Comparison of hybrid Hall thruster model to experimental measurements. *Physics of Plasmas*, 13(8):083505, 2006.

[71]Ch. Wang, L. Wei, and D. Yu. A basic predator-prey type model for low frequency discharge oscilations in Hall thrusters. *Contributions to Plasma Physics*, 51(10):981–988, 2011.

[72]K. Vladimir, D. Grdlichko, V. Kozlov, A. Lazourenko, G. Popov, and A. Skrylnikov. Local plasma parameter measurements by nearwall probes inside the SPT accelerating channel under thruster operation with Kr. In *38th Joint Propulsion Conference and Exhibit*, paper AIAA 2002-4108, Indianapolis, IN, USA, July 7-10, 2002. American Institute of Aeronautics and Astronautics, https://www.aiaa.org.

[73]K. Vladimir, V. Kozlov, A. Skrylnikov, L. Umnitsin, V. Svotina, A. Bouchoule, and M. Prioul. Investigation of the local plasma parameter distributions in the SPT accelerating channel under increased discharge voltages. In *29th International Electric Propulsion Conference*, paper IEPC 2005-004, Princeton, NJ, USA, October 31 - November 4, 2005. Electric Rocket Propulsion Society, https://erps.spacegrant.org.

[74]Y. Raitses, D. Staack, M. Keidar, and N. J. Fisch. Electron-wall interaction in Hall thrusters. *Physics of Plasmas*, 12(5):057104, 2005.

[75]Y. Raitses, D. Staack, A. Smirnov, and N. J. Fisch. Space charge saturated sheath regime and electron temperature saturation in Hall thrusters. *Physics of Plasmas*, 12(7):073507, 2005.

[76]R. D. Hazeltine and J. D. Meiss. *Plasma confinement*. Redwood City, CA: Addison-Wesley, 1992.

[77]G. J. M. Hagelaar, J. Bareilles, L. Garrigues, and J. P. Boeuf. Role of anomalous electron transport in a stationary plasma thruster simulation. *Journal of Applied Physics*, 93(1):67–75, 2003.

[78]S. Barral and J. Miedzik. Numerical investigation of closed-loop control for Hall accelerators. *Journal of Applied Physics*, 109(1):013302, 2011.

[79]S. Barral, J. Kaczmarczyk, J. Kurzyna, and M. Dudeck. Active control and excitation of breathing oscillations in a Hall thruster with a fast digital signal processor. In *33rd International Electric Propulsion Conference*, paper IEPC 2013-339, Washington D. C., USA, October 7-10, 2013. Electric Rocket Propulsion Society, https://erps.spacegrant.org.

[80]F. Cichocki, A. Domínguez-Vázquez, M. Merino, and E. Ahedo. 3D simulations of a magnetized Hall effect thruster plume. In *36th International Electric Propulsion Conference*, paper IEPC 2019-460, Vienna, Austria, 2019. Electric Rocket Propulsion Society, https://erps.spacegrant.org.

[81]A. Anton and E. Ahedo. Contour algorithms for a Hall thruster hybrid code. In *42nd Joint Propulsion Conference and Exhibit*, paper AIAA 2006-4834, Sacramento, CA, USA, July 9-12, 2006. American Institute of Aeronautics and Astronautics, https://www.aiaa.org.

[82]D. Escobar, A. Antón, and E. Ahedo. Simulation of high-specific-impulse and double-stage Hall thrusters. In *29th International Electric Propulsion Conference*, paper IEPC 2005-040, Princeton, NJ, USA, October 31 - November 4, 2005. Electric Rocket Propulsion Society, https://erps.spacegrant.org.